

# Probing the Progenitors of Type Ia Supernovae using Circumstellar Material Interaction Signatures

Peter Clark,<sup>1,2</sup> Kate Maguire,<sup>3</sup> Mattia Bulla,<sup>4</sup> Lluís Galbany,<sup>5</sup> Mark Sullivan,<sup>6</sup>  
Joseph P. Anderson<sup>7,8</sup> and Stephen J. Smartt<sup>2</sup>

<sup>1</sup>*Institute of Cosmology and Gravitation, University of Portsmouth, Portsmouth PO1 3FX, UK.*

<sup>2</sup>*Astrophysics Research Centre, School of Mathematics and Physics, Queen's University Belfast, Belfast BT7 1NN, UK.*

<sup>3</sup>*School of Physics, Trinity College Dublin, Dublin 2, Ireland.*

<sup>4</sup>*The Oskar Klein Centre, Department of Astronomy, Stockholm University, AlbaNova, SE-106 91, Stockholm, Sweden.*

<sup>5</sup>*Institute of Space Sciences (ICE, CSIC), Campus UAB, Carrer de Can Magrans, s/n, E-08193 Barcelona, Spain.*

<sup>6</sup>*School of Physics and Astronomy, University of Southampton, Southampton, SO17 1BJ.*

<sup>7</sup>*European Southern Observatory, Alonso de Córdova 3107, Casilla 19, Santiago, Chile*

<sup>8</sup>*Millennium Institute of Astrophysics, Nuncio Monsenor Sotero Sanz 100, Of. 104, Providencia, Santiago, Chile*

Accepted 2021 July 13. Received 2021 July 13; in original form 2021 April 30

## ABSTRACT

This work aims to study different probes of Type Ia supernova progenitors that have been suggested to be linked to the presence of circumstellar material (CSM). In particular, we have investigated, for the first time, the link between narrow blueshifted Na I D absorption profiles and the presence and strength of the broad high-velocity Ca II near infrared triplet absorption features seen in Type Ia supernovae around maximum light. With the probes exploring different distances from the supernova; Na I D  $> 10^{17}$  cm, high-velocity Ca II features  $< 10^{15}$  cm. For this, we have used a new intermediate-resolution X-shooter spectral sample of 15 Type Ia supernovae. We do not identify a link between these two probes, implying either that, one (or both) is not physically related to the presence of CSM or that the occurrence of CSM at the distance explored by one probe is not linked to its presence at the distance probed by the other. However, the previously identified statistical excess in the presence of blueshifted (over redshifted) Na I D absorption is confirmed in this sample at high significance and is found to be stronger in Type Ia supernovae hosted by late-type galaxies. This excess is difficult to explain as being from an interstellar-medium origin as has been suggested by some recent modelling, as such an origin is not expected to show a bias for blueshifted absorption. However, a circumstellar origin for these features also appears unsatisfactory based on our new results given the lack of link between the two probes of CSM investigated.

**Key words:** circumstellar matter – supernovae:general – distance scale.

## 1 INTRODUCTION

Type Ia supernovae (SNe Ia) are the explosions of white dwarfs in binary systems, play a major role in our understanding of the expansion rate of the Universe and are essential for constraining the properties of dark energy to high precision (e.g., Scolnic et al. 2018). Despite this, there are still major gaps in our understanding of their underlying progenitor systems. While the observed rate of SNe Ia is measurable by sky surveys (e.g., Li et al. 2011; Frohmaier et al. 2019), the rate of the underlying progenitor channels is much more uncertain, with the likely possibility that there is more than one way to make a SN Ia (e.g., Maoz et al. 2014; Jha et al. 2019). Classical SN Ia models involve an exploding white dwarf that is close to the Chandrasekhar mass, which has accreted matter from a non-degenerate companion star and resulting in a runaway thermonuclear reaction (Whelan et al. 1973). Models involving the ex-

plosion of sub-Chandrasekhar mass white dwarfs have also gained popularity and the explosion can occur through a violent or dynamical merger (Pakmor et al. 2010) or the triggering of a He-shell on the white dwarf surface, which results in a detonation of the core ('double-detonation'; Taam 1980; Livne & Arnett 1995; Shen & Bildsten 2009; Fink et al. 2010).

One observational method that has been used to distinguish between potential SN Ia progenitor scenarios is the presence of circumstellar material (CSM), which is thought to be more likely in the case of a non-degenerate companion star (Hachisu et al. 1999a,b), although may be present in some merger scenarios (e.g., Raskin & Kasen 2013). Time-varying blueshifted Na I D absorption features have been identified in some SNe Ia (Patat et al. 2007; Simon et al. 2009; Blondin et al. 2009, 2017; Stritzinger et al. 2010; Sternberg et al. 2014), with the interpretation that these were due to outflowing (hence blueshifted) CSM close to the SN (distances of  $\sim 10^{17}$

cm) and not interstellar material (ISM). Additionally, an excess of blueshifted compared to redshifted Na I D absorption features has been identified in larger SN Ia samples, consistent with a CSM origin in  $\sim 20\%$  of SNe Ia (Sternberg et al. 2011; Maguire et al. 2013).

Potential links between the presence of blueshifted Na I D absorption and the properties of the SNe Ia themselves (Si II velocity, colour at maximum) have been suggested (e.g., Foley et al. 2012; Maguire et al. 2013; Phillips et al. 2013). SNe Ia displaying blueshifted Na I D absorption are associated with redder  $B-V$  colours at maximum and in some cases also have higher Si II velocities (but this trend is not seen in all studies e.g., Maguire et al. 2013). A link between SNe Ia showing high-velocity Si II features and redder  $B-V$  colours at maximum was also previously suggested by Wang et al. (2009). SNe Ia with stronger Na I D absorption in low-resolution spectra also have a preference for redshifted late-time emission line velocities (Förster et al. 2012).

Phillips et al. (2013) found that SNe Ia displaying blueshifted Na I D have stronger Na I column densities compared to what would be expected from their colour-derived extinction. This was not the case for their non-blueshifted sample, where the extinction and Na I column densities followed the Milky Way relation. This study concluded that the strong Na I column densities for the blueshifted Na I D sample was potentially evidence for outflowing CSM from these systems but there does not appear to be a direct relation; some SNe Ia that are identified as having time-varying Na I D (thought to be a clear indicator of CSM interaction) do not follow this relation.

The ratio of total-to-selective extinction,  $R_V$ , measured in the Milky Way has a typical value of  $\sim 3.1$  (Fitzpatrick 1999), though a range of values are observed (Mörtsell 2013 found a value  $\sim 3$  with an uncertainty of around 10%, whereas Nataf et al. 2013 find a  $R_V$  value of 2.5 in the direction of the galactic core). Much lower values ( $R_V < 2$ ) have been measured for some highly extinguished SNe Ia (e.g., Amanullah et al. 2014; Burns et al. 2014), with these measurements confirmed through spectropolarimetry (Patat et al. 2015; Zelaya et al. 2017). However, whilst not measuring the parameter in the same way, larger cosmological samples of normal SNe Ia have identified a range of  $R_V$ , from  $R_V \leq 2$  (e.g., Astier et al. 2006; Conley et al. 2007), to values closer to 3 (e.g., Fink et al. 2010; Mandel et al. 2011). The cause of the low  $R_V$  values seen in some SNe Ia is debated. Some studies have suggested it could be due to multiple scattering in CSM around the SNe Ia (Wang 2005; Goobar 2008; Amanullah & Goobar 2011), due to enhanced Na abundances in the CSM (Phillips et al. 2013). Other studies have concluded that it is mainly produced in the ISM (Bulla et al. 2018a,b), where cloud-cloud collisions from the radiation pressure generated by the exploding SNe themselves may produce smaller dust grains (Hoang 2017; Giang et al. 2020).

High-velocity components in the Ca II NIR triplet absorption feature are observed in nearly all SNe Ia spectra obtained around maximum light (Hatano et al. 1999; Gerardy et al. 2004; Mazzali et al. 2005; Childress et al. 2013a,b; Maguire et al. 2014), though the strengths of such components vary significantly between objects. The origin of these high-velocity components (with velocities a few thousand  $\text{km s}^{-1}$  greater than the photospheric components) is unclear but it has been proposed that the high-velocity components of the Ca II NIR triplet could have contributions from CSM (at distances of  $\sim 10^{14}$  cm) (Gerardy et al. 2004; Mazzali et al. 2005; Quimby et al. 2006; Tanaka et al. 2008) or they may be intrinsic to the SN ejecta (Branch et al. 2006; Blondin et al. 2012). If a clear relation between blueshifted Na I D absorption and high velocity Ca II absorption were to be established, it would be a strong indi-

cation of local CSM interaction during the early phases of SNe Ia evolution.

The focus of this paper is to investigate the link between two potential probes of the presence of CSM around SNe Ia; the presence of blueshifted Na I D absorption features and the properties of Ca II high-velocity features. We do this using a new sample of intermediate-resolution spectra of SNe Ia around maximum combined with the literature samples of Sternberg et al. (2011) and Maguire et al. (2013). Section 2 outlines the observations and reduction techniques employed in the construction of the dataset used in this work, while Section 3 details the analysis of the sample of spectra obtained, along with their complementary photometric observations and host galaxy measurements. Section 4 describes the main results and Section 5 discusses the implications of these results in the context of the progenitors of SNe Ia and previous studies. Section 6 presents a summary of our main findings. Throughout this paper, we assume a Hubble constant,  $H_0$  of  $70 \text{ km s}^{-1} \text{ Mpc}^{-1}$  and adopt a standard cosmology with  $\Omega_M=0.27$  and  $\Omega_\Lambda=0.73$ .

## 2 OBSERVATIONS AND DATA REDUCTION

In this section, we describe the new data sample used in this work of maximum light X-shooter spectra of 16 SNe Ia. In Section 2.1, we describe the reduction process and telluric correction. In Section 2.2, we discuss the estimates of the light curve properties (light curve width, colour at maximum), as well as the spectroscopic sub-classification of each SN Ia in the sample. In Section 2.3, we discuss additional literature objects that are included to increase the sample size.

### 2.1 X-shooter spectroscopic observations

The primary dataset used in this work consists of maximum light (within approx. one week of peak) medium-resolution X-shooter spectroscopy of 16 SNe Ia with wavelength coverage of  $\sim 3000$  to  $25000 \text{ \AA}$  across three arms (UVB, VIS, NIR) (Vernet et al. 2011). The SNe were chosen for observation with X-shooter in an unbiased manner, using the same criteria as Maguire et al. (2013) i.e., the target SNe Ia had already been spectroscopically classified and reported on the Transient Name Server (TNS) prior to maximum light to eliminate the risk of contamination from other types of transient with a redshift  $< 0.03$  to enable a high signal to noise spectrum to be obtained. A summary of the sample, including their discovery information and properties of their host galaxies, is presented in Table 1.

The X-shooter spectra were reduced in a standard manner using the ESO Reflex reduction pipeline to produce flux-calibrated spectra (Modigliani et al. 2010; Freudling et al. 2013). Additional telluric corrections were applied to the VIS and NIR arm of the majority of the sample with the MOLECFIT software (Smette et al. 2015; Kausch et al. 2015). A telluric correction was not applied for 2 SNe Ia (SNe 2017hn and 2017bkc) for the NIR arm because of low signal-to-noise (S/N). SN 2017guh was consistent with the core of its host galaxy and suffered from significant host galaxy contamination and therefore is removed from further analysis. The spectra were corrected for Galactic extinction using the  $E(B-V)$  values from Schlafly & Finkbeiner (2011) and the extinction law of Fitzpatrick (1999). The definition of the redshift of each SN is central to this analysis and is discussed further in Section 3.1.1.

**Table 1.** Discovery and host galaxy information for the SN Ia sample. The discovery survey is that reported on the TNS. Two redshifts are listed, the heliocentric value from NED along with the final adopted redshift. The redshift calibration method for each adopted redshift is listed as either emission features (a mean value if there is more than one feature) seen in the X-shooter spectra or if no lines were seen, the value from NED is used.

SN name	Discovery survey	Host galaxy name	Host morphology <sup>a</sup>	NED host $z$	Adopted $z$	$z$ calibration method
SN 2016hvl	ATLAS <sup>b</sup>	UGC 03524	S <sup>1</sup>	0.0131	0.0131	H $\alpha$
SN 2016ipf*	ATLAS	2MASX J08071352+0540566	E <sup>3</sup>	0.021	0.0206	H $\alpha$
SN 2017hm	ASAS-SN <sup>b</sup>	MCG-02-30-003	Sb <sup>1</sup>	0.0213	0.0219	H $\alpha$
SN 2017hn	POSS <sup>c</sup>	UGC 08204	S0 <sup>1</sup>	0.02385	0.02385	NED
SN 2017yv	ASAS-SN	ESO 375-G018	S <sup>3</sup>	0.0156	0.0158	H $\alpha$ + N II
SN 2017awz	ATLAS	MCG+04-26-033	S <sup>2</sup>	0.022	0.0221	H $\alpha$ + N II
SN 2017azw	ASAS-SN	ESO 015-G010	Dwarf <sup>3</sup>	0.02	0.02	NED
SN 2017bkc	ASAS-SN	J17503055-0148023	S <sup>2</sup>	0.0174	0.0163	H $\alpha$
SN 2017cbv**	DLT40 <sup>d</sup>	NGC 5643	Sc <sup>1</sup>	0.003999	0.003999	NED
SN 2017ckq	ATLAS	ESO 437-G056	Sbc <sup>1</sup>	0.0099	0.0098	H $\alpha$
SN 2017ejb	DLT40	NGC 4696	E <sup>1</sup>	0.00987	0.00987	NED
SN 2017fgc	DLT40	NGC 0474	S0 <sup>1</sup>	0.007722	0.007722	NED
SN 2017fzw	DLT40	NGC 2217	S0 <sup>1</sup>	0.0054	0.0054	NED
SN 2017gah	ATLAS	NGC 7187	S0 <sup>1</sup>	0.008906	0.008906	NED
SN 2017guh***	ASAS-SN	ESO 486-G019	S0 <sup>1</sup>	0.015427	0.015427	NED
SN 2017gvp	ASAS-SN	UGC 12739	S <sup>1</sup>	0.023	0.0229	H $\alpha$

<sup>a</sup>Host galaxy morphology source: <sup>1</sup>de Vaucouleurs et al. (1991), <sup>2</sup>visually classified as part of this work, <sup>3</sup>Lauberts et al. (1981).

<sup>b</sup>ATLAS: Asteroid Terrestrial-impact Last Alert System (Tonry et al. 2018)

<sup>c</sup>ASAS-SN: All-Sky Automated Survey for Supernovae (Shappee et al. 2014).

<sup>d</sup>POSS: Puckett Observatory Supernova Search (<http://cometwatch.com/supernovasearch/discoveries.html>).

<sup>e</sup>DLT40: Sub-day cadence SN search of galaxies at  $D < 40$  Mpc (Sand et al. 2018).

\*No heliocentric host redshift is available on NED, with the host  $z$  taken from the original TNS classification report

\*\*SN 2017cbv is notable for having a significant early excess in the bluer bands of its light curve (Hosseinzadeh et al. 2017). It was also investigated by Ferretti et al. (2017) exploring if it displayed any time variable Na I D absorption features - none were detected.

\*\*\*SN 2017guh is excluded from further analysis due to strong host galaxy contamination.

**Table 2.** Summary table of the SN sub-type classification, light curve and spectral properties.

SN name	Sub-type <sup>a</sup>	Light curve stretch	$B - V$ at peak	$B - V_{\text{spec}}^b$	MJD <sup>c</sup> of spectrum	Spectral phase (d) <sup>d</sup>	Na I D profile <sup>e</sup>	Ca II H&K profile <sup>e</sup>	Na I D <sub>2</sub> pEQW total ( $\text{\AA}$ ) <sup>f</sup>	Na I D <sub>2</sub> pEQW blue ( $\text{\AA}$ ) <sup>g</sup>
SN 2016hvl	Ia-91T	1.14 ± 0.05	–	−0.14 ± 0.23	57702.29	−7.80 ± 0.46	Blue	Inconclusive*	0.157 ± 0.023	0.143 ± 0.012
SN 2016ipf	Ia	–	–	−0.08 ± 0.23	57725.28	−3 ± 1	No Abs.	Inconclusive*	–	0.018 ± 0.018
SN 2017hm	Ia	1.11 ± 0.03	–	0.11 ± 0.23	57775.33	2.94 ± 0.15	Blue	Inconclusive*	0.107 ± 0.022	0.083 ± 0.010
SN 2017hn	Ia-91T	1.44 ± 0.22	–	0.23 ± 0.23	57773.32	2.46 ± 2.36	No Abs.	Inconclusive*	–	–
SN 2017yv	Ia	1.01 ± 0.20	–	0.19 ± 0.23	57797.22	2.81 ± 0.72	Blue	Blue	0.503 ± 0.005	0.400 ± 0.003
SN 2017awz	Ia-91T	0.95 ± 0.11	–	0.14 ± 0.23	57816.21	4.01 ± 0.60	Blue & Red	Blue & Red	1.235 ± 0.014	0.797 ± 0.008
SN 2017azw	Ia	–	–	−0.05 ± 0.23	57816.02	1 ± 1	No Abs.	No Abs.	–	–
SN 2017bkc	Ia	–	–	0.23 ± 0.23	57816.36	5 ± 3	No Abs.	No Abs.	0.066 ± 0.022	0.009 ± 0.018
SN 2017cbv	Ia	1.11 ± 0.02	0.04 ± 0.02	−0.23 ± 0.23	57837.15	−2.82 ± 0.04	Red	Red	0.036 ± 0.010	0.010 ± 0.004
SN 2017ckq	Ia	1.02 ± 0.03	0.00 ± 0.04	0.00 ± 0.23	57853.06	2.42 ± 0.11	Blue	Blue	0.069 ± 0.022	0.019 ± 0.011
SN 2017ejb	Ia-91bg	0.73 ± 0.03	0.28 ± 0.06	0.45 ± 0.23	57913.05	−2.84 ± 0.07	No Abs.	No Abs.	–	–
SN 2017fgc	Ia	0.92 ± 0.02	–	0.22 ± 0.23	57961.32	2.15 ± 0.17	No Abs.	Blue & Red	–	–
SN 2017fzw	Ia	0.74 ± 0.01	0.33 ± 0.06	0.16 ± 0.23	57983.39	−3.99 ± 0.13	No Abs.	No Abs.	–	–
SN 2017gah	Ia	0.82 ± 0.01	0.13 ± 0.02	0.30 ± 0.23	57982.26	−2.74 ± 0.08	No Abs.	Inconclusive*	0.015 ± 0.018	0.022 ± 0.010
SN 2017gvp	Ia	1.19 ± 0.15	–	0.02 ± 0.23	58026.10	−2.83 ± 0.75	Blue & Red	Blue	0.692 ± 0.018	0.374 ± 0.007

<sup>a</sup>Sub-type classification based on SNID (Blondin & Tonry 2007).

<sup>b</sup> $B - V$  colour calculated from X-shooter spectra at that phase.

<sup>c</sup>Modified Julian Date of start time of first X-shooter spectral exposure.

<sup>d</sup>Relative to  $B$ -band maximum. Where no light curve is available, the phase was estimated from the best-fit SNID spectral template.

<sup>e</sup>The profiles are classified as having components that are ‘blueshifted’, ‘redshifted’, ‘blue and redshifted’ or ‘no absorption’.

<sup>f</sup>Na I D<sub>2</sub> pEQW in the range  $-200 - 200 \text{ km s}^{-1}$ . Features where the emission is consistent with spectral noise are set to zero.

<sup>g</sup>Na I D<sub>2</sub> pEQW in the range  $-200 - 0 \text{ km s}^{-1}$ . Features where the emission is consistent with spectral noise are set to zero.

\*No consistent absorption - absorption was seen from only one of the Ca II lines.

## 2.2 Light curve properties and spectral classification

Light curves from the Asteroid Terrestrial-impact Last Alert System (ATLAS Tonry et al. 2018; Smith et al. 2020) sky survey were used to constrain the photometric properties of 9 events in the sample (as indicated in Table 2). Photometric information for these objects can be retrieved from the ATLAS forced photometry server (Shingles

et al. 2021). A measure of the light curve width (‘stretch’) was estimated using the SiFTO light curve fitting code (Conley et al. 2008) for these events. The maximum light  $B - V$  colour was also estimated using SiFTO for two events (SN 2017ckq, SN 2017gah) with multi-band (ATLAS cyan and ATLAS orange) photometry around maximum light. For three objects in the sample, photometry

from the literature was fit using SiFTO: SN 2017cbv (Hosseinzadeh et al. 2017), SN 2017ejb and SN 2017fzw (Galbany et al. in prep.) The ‘stretch’ values, along with available  $B-V$  colours at maximum, for the sample are presented in Table 2. The stretch range ( $\sim 0.82-1.44$ ) is consistent with that found for the low- $z$  Palomar Transient Factory (PTF) SN Ia sample (Maguire et al. 2014).

Since light curve colour measurements were only available for five events,  $B-V$  colours around maximum were also estimated using the X-shooter spectra. These spectra were integrated through  $B$  and  $V$  band filters to obtain the colour at the phase of the spectrum. We have excluded SN 2016hvl from our spectral colour comparisons because its spectral phase ( $-7.8 \pm 0.46$  d) is significantly earlier than the rest of the sample of  $-4$  to  $+5$  d from peak.

The instrument response of X-shooter is relatively stable, with an estimated relative flux uncertainty of five per cent across the spectrum (Vernet et al. 2011). Since we are only interested here in the colour, the absolute flux calibration is not relevant. As a sanity check on the magnitude of this uncertainty, we have compared the photometric  $B-V$  values obtained at peak against the values measured from X-shooter spectra for four events (SN 2012cg, SN 2012ht, LSQ12dbr, SN 2013aj) from Maguire et al. (2013) and find agreement within the uncertainties for the four events. For the five events in our sample with both photometric and spectroscopic colour measurements, we have also compared these values and find that they are in agreement except for a slight discrepancy ( $\sim 1-\sigma$ ) for SN 2017cbv, which we attribute to the earlier phase of its spectrum. To quantify the additional uncertainty that will be introduced to changes in phase, we have estimated the colour change within a phase range of  $\pm 4$  d for the well-studied event SN 2017cbv (Hosseinzadeh et al. 2017) to be  $\sim 0.1$  mag, which is also consistent with the range for SN 2011fe and SN 2012cg (see Figure 2 of Hosseinzadeh et al. 2017). We have added this additional uncertainty due to phase in quadrature (see Table 2).

The SNe Ia in the sample were sub-classified using the SN Identification SNID code (Blondin & Tonry 2007) applied to their X-shooter spectra. The bulk of the sample (11/15) were classified as ‘normal’ SNe Ia, three as 91T-like events, and one as a 91bg-like event (see Table 2). SN 2017fzw is classified as a ‘normal’ SN Ia based on the SNID comparison but has some unusual properties, as will be discussed further in Galbany et al. (in prep.).

### 2.3 Literature comparison sample

In order to increase the number of objects available for inclusion in the statistical analysis of this work, the 15 newly presented objects are supplemented by the inclusion of the combined dataset described in Maguire et al. (2013). This additional dataset consists of 16 SNe Ia observed with X-shooter and 16 SNe Ia from Sternberg et al. (2011) with similar intermediate-resolution spectra around maximum light. Our combined sample (referred to as the ‘full’ sample) consists of 47 SNe Ia. We note that the sample of Sternberg et al. (2011) has a weak selection effect, with six of the objects selected based on identification of strong narrow Na I D absorption features e.g., SN 2006X.

## 3 ANALYSIS

In this section, we describe the analysis performed to calibrate the spectra to the rest frame and determine the presence of blueshifted material (Section 3.1), the host galaxy morphologies and stellar

mass measurements of the sample (Section 3.2), and the measurements of the broad SN absorption components of Si II and Ca II.

### 3.1 Identification of narrow absorption features

As the narrow features displayed by the Na I D and Ca II H&K lines are at low velocities, displaying shifts of only a few hundred  $\text{km s}^{-1}$  from their expected rest positions (Patat et al. 2007), accurate redshift calibration is key in determining if any observed features are red or blueshifted. Any contaminating absorption features produced by unrelated interstellar material in the host galaxy would also be expected to be detected within a few hundred  $\text{km s}^{-1}$  of the SN, given the typical velocity distributions of material in galaxies. Such contamination is expected to produce an equal amount of both ‘blue’ and ‘redshifted’ absorption features (with respect to the SN rest-frame) with potential SN-generated features being exclusively blueshifted, due to their origin in out-flowing stellar material and the associated line of sight effects (but see Hoang 2017).

#### 3.1.1 Redshift and zero-velocity calibration

To determine the accurate rest frame of each SN, measurements were made using host galaxy emission features identified in the two-dimensional spectral frames, close to the SN position. The host galaxy lines used were the H $\alpha$  and N II 6583 Å due to their proximity to the most important feature in this analysis, Na I D. The lines used in the determination of the redshift for each event and the measured redshift is given in Table 1. For seven events in the sample, no host galaxy features could be identified in the X-shooter spectra. This was due to either the SN having a significant offset from its host and/or the host being an early-type galaxy that lacks strong emission features. This could potentially result in larger uncertainties due to the lack of an accurate rest frame correction at the SN position. However, for the seven events without identified host features, none showed absorption profiles for Na I D - thus these cases are unaffected. The adopted redshift in Table 1 for these events is the heliocentric redshift retrieved from NED<sup>1</sup>.

Based on these redshifts, the ‘position’ of the zero-velocity for each spectrum can be obtained and the classification of the Na I D and Ca II H&K features into ‘redshifted’, ‘blueshifted’, ‘red and blueshifted’ or ‘no absorption’ with respect to the zero rest-frame position from the host galaxy lines can be made. This schema mirrors that used in Maguire et al. (2013), which was modified from that of Sternberg et al. (2011). We again note that those SNe calibrated using the host redshifts have increased uncertainties due to galactic rotation effects (though no SNe in this sample with observed Na I D absorption was calibrated in this manner). Additionally if the material responsible for producing the narrow galaxy lines is located somewhat in front or behind the true SN position the calibration will also be affected though these offsets are expected to be small with the use of local lines from the 2D spectral frames. Figures 1 and 2 show the SNe with ‘blueshifted’ and ‘red and blueshifted’ Na I D absorption profiles, Figure 3 shows an event (SN 2017cbv) identified with a redshifted Na I D absorption profile (consistent with higher resolution spectra obtained with UVES Ferretti et al. 2017), and Figs. 4 and 5 show the objects with ‘no absorption’ components of Na I D. The Ca II H&K features are shown for comparison - in

<sup>1</sup> The NASA/IPAC Extragalactic Database (NED) is operated by the Jet Propulsion Laboratory, California Institute of Technology, under contract with the National Aeronautics and Space Administration.



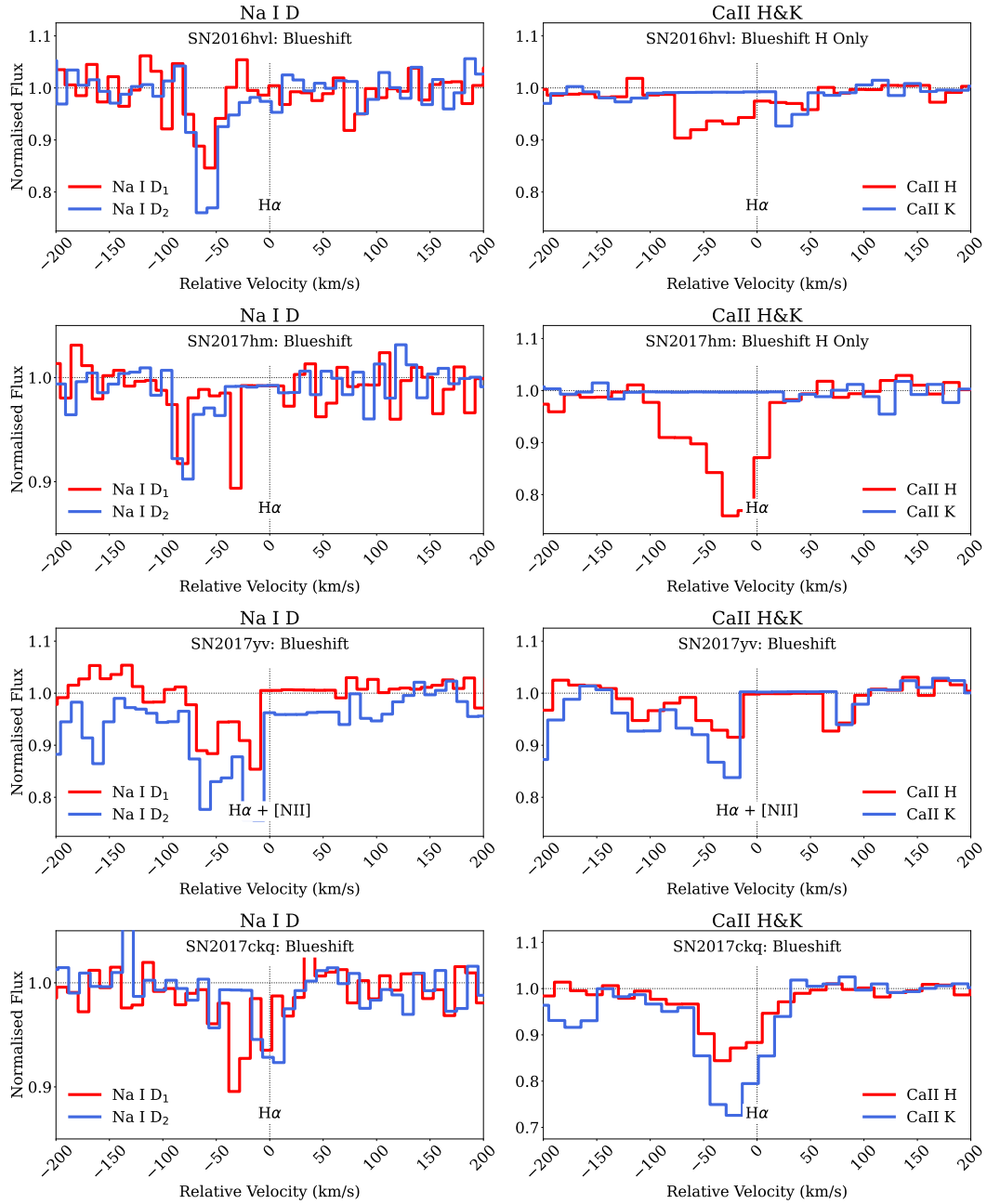


**Figure 1.** Na I D (left panels) and Ca II H&K (right panels) regions of objects displaying blueshifted Na I D absorption features. The method of redshift classification is also indicated below the spectra, with the galactic emission lines used.

studies of time-varying narrow features, (e.g., Patat et al. 2007) the Ca II features are not seen to vary, which is suggested to be due to their higher ionisation potential compared to Na I D. We find that the Ca II classifications are generally in agreement with those of the Na I D, with just two having different classifications, SN 2017fgc where the Ca II H&K feature had blue and redshifted absorption while the Na I D had no absorption and SN 2017gvp where the Ca II H&K had blueshifted only absorption and the Na I D had blue and red. A similar small number of inconsistencies between these features was also identified in Maguire et al. (2013). As in previous studies, we focus on the Na I D features and only use the Ca II H&K feature for confirming weak Na I D features.

### 3.1.2 Continuum calibration and pseudo-equivalent widths

To make measurements of the pseudo-equivalent widths (pEQWs) of the narrow Na I D features, any continuum offset needs to be removed. This was done using a linear interpolation between uncontaminated regions on either side of the Na I D feature. The pEQWs of each feature were then measured following the method of Förster et al. (2012). Following previous works, the measurement of the stronger of the two lines making up the Na I D doublet (Na I D<sub>2</sub>) is used as the measure of the feature’s overall strength.

To gain an understanding of overall absorption strength, as well as the strength of only the blueshifted absorption component, the measurement of the pEQW has been made in two velocity re-

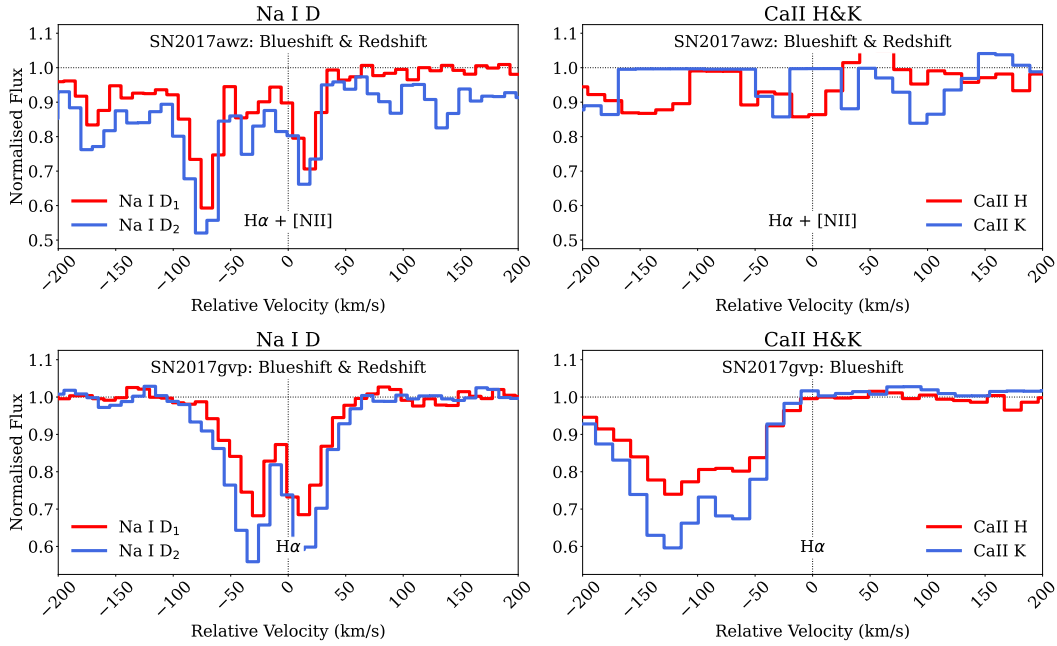


**Figure 2.** Na I D (left panel) and Ca II H&K (right panel) regions of objects displaying blue and redshifted Na I D absorption features. The method of redshift classification is also indicated below the spectra, with the galactic emission lines used.

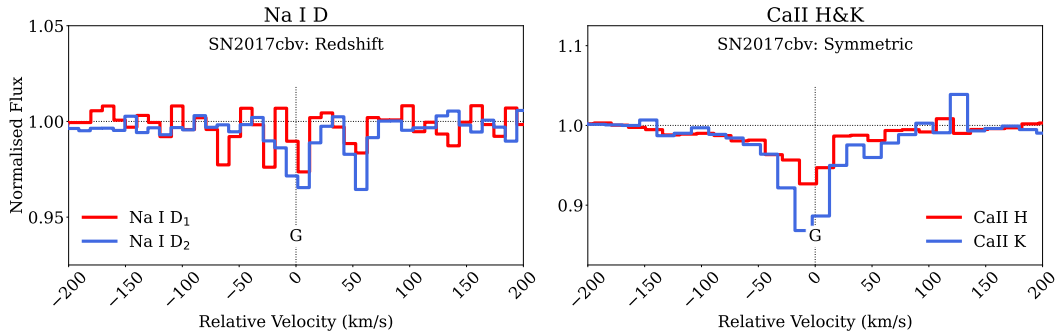


**Figure 3.** Na I D (left panel) and Ca II H&K (right panel) regions of SN 2017cbv, the one object displaying redshifted Na I D absorption features. The method of redshift classification is also indicated below the spectra, with ‘G’ for a galactic redshift estimate from the literature. This classification is supported by the UVES observations described in (Ferretti et al. 2017)

gions relative to the calibrated position of zero velocity. The overall strength of the feature measured in the region  $-200 - +200 \text{ km s}^{-1}$  (‘total pEQW’) with the pEQW of the blueshifted component measured from  $-200 - 0 \text{ km s}^{-1}$ . These values are tabulated in Table 2. Some previous studies have used larger velocity ranges in the calculation of the pEQWs of Na I D, such as Förster et al. (2012) who measured the features out to  $\pm 300 \text{ km s}^{-1}$ . However, the higher resolution of the X-shooter spectra allows a narrower region to be used.

Both these pEQW measurements have been made for the 15 new SNe Ia explored in this work, including those for which a Na I D absorption feature could not be visually identified, to serve as a confirmation of the non-detection of these features. The regions selected for the continuum were varied randomly within  $15 \text{ \AA}$  of their initially selected locations and the calculation repeated for a total of 5000 measurements to provide a measure of the uncertainty associated with the pEQW measurement. The pEQW values for the literature sample were taken from Maguire et al. (2013), which were obtained using an analogous method.

## 3.2 Host galaxy analysis

To search for correlations between the properties of SNe Ia and their environments, that could in turn be related to differing progenitor scenarios, we perform an analysis of the host properties of our SN Ia sample. This work uses both visual morphological classification of the host galaxies of the SN Ia sample, along with photometric determinations of the total stellar mass of the hosts, where suitable data are available. We also calculate the projected distance between each SN and the nucleus of its host.

### 3.2.1 Host morphological classification

Host morphological classifications for the SN Ia sample were retrieved from NED and are sourced from the classification catalogues of Lauberts et al. (1981) and de Vaucouleurs et al. (1991). For two objects (SN 2017awz, SN 2017bkc), visual classification as spiral galaxies was performed as part of this work. These morphological classifications are given in Table 1 as spiral (‘S’) and sub-

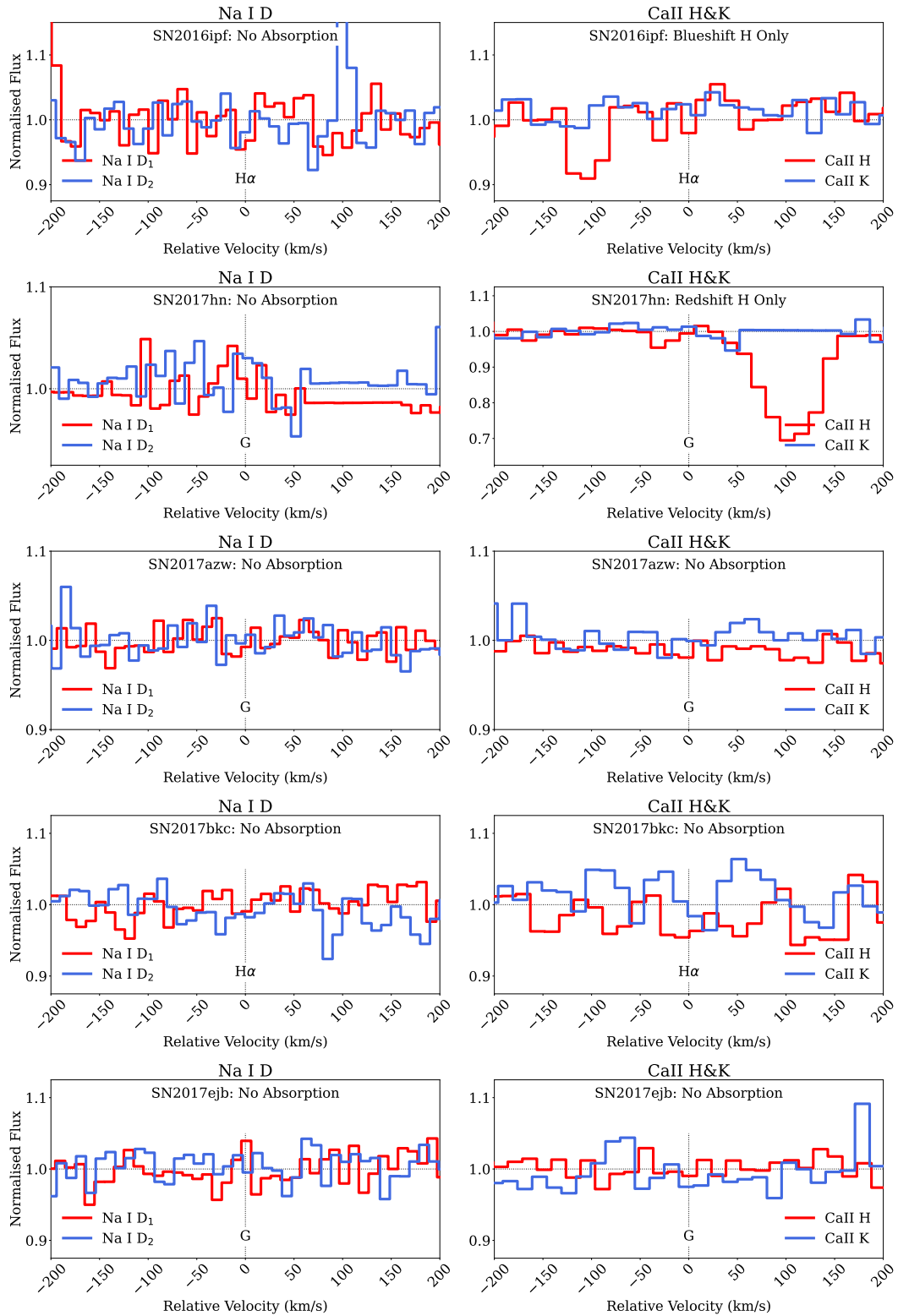


**Figure 4.** Na I D (left panel) and Ca II H&K (right panel) regions of objects displaying no Na I D absorption features. The method of redshift classification is also indicated below the spectra with the galactic emission lines used or 'G' for a galactic redshift estimate from the literature.

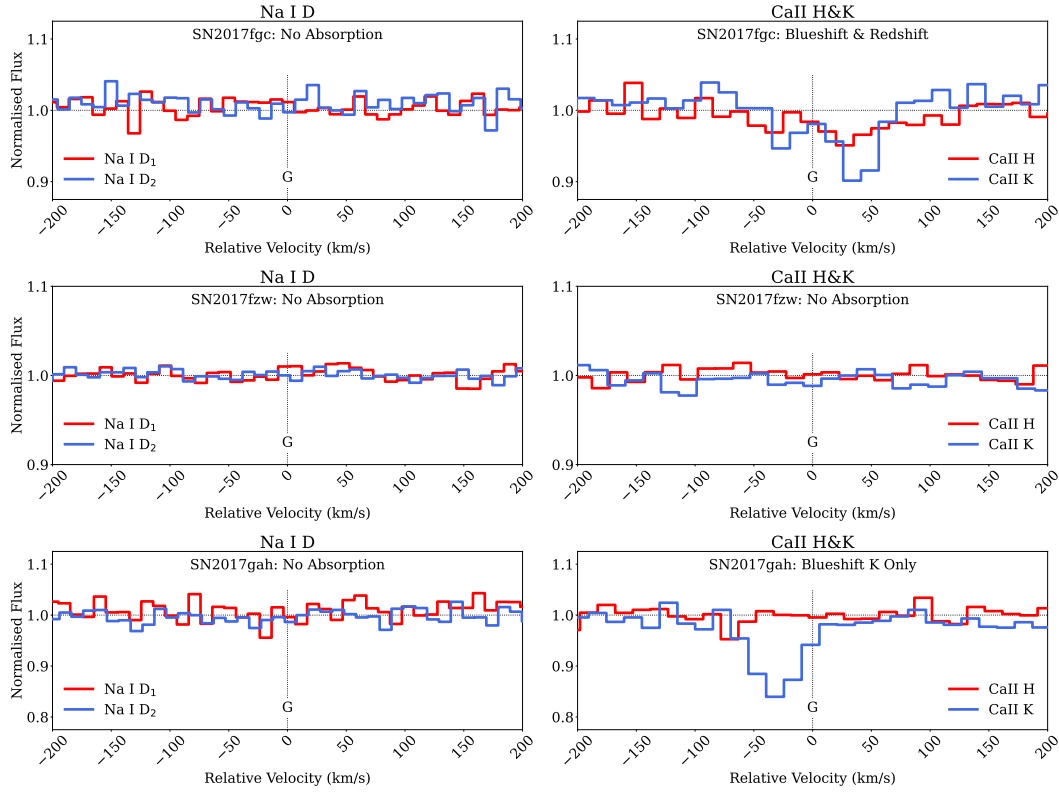


**Figure 5.** Na I D (left panels) and Ca II H&K (right panels) regions of additional objects displaying no Na I D absorption features. The method of redshift classification is also indicated below the spectra with ‘G’ for a galactic redshift estimate from the literature.

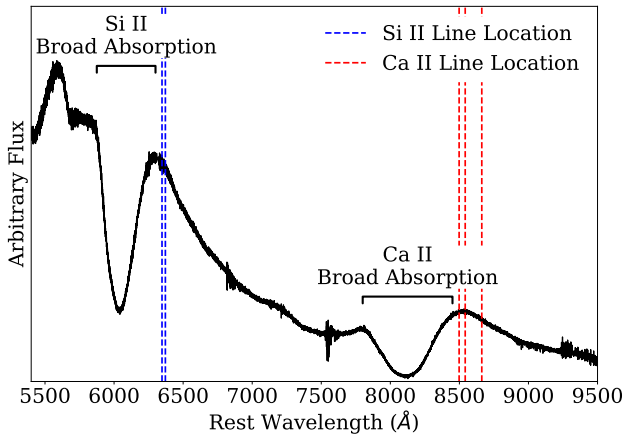


**Figure 6.** Plot of the 5750–9500 Å region of SN 2017fgc with the Si II 6355 Å and Ca II NIR triplet absorption features identified. The vertical dashed blue lines represent the rest wavelengths of the Si II doublet and the vertical dashed red lines the rest wavelengths of the Ca II NIR triplet.

classifications (‘S0’, ‘Sa’, ‘Sab’, ‘Sb’, ‘Sbc’, ‘Sc’), elliptical (‘E’), or dwarf.

Morphological classifications for the hosts of the SNe included in the combined sample of objects from literature were adopted from their description in [Sternberg et al. \(2011\)](#) or [Maguire et al. \(2013\)](#), apart from four cases, where updated classifications were used. These objects are SN 2008C, which is updated from ‘S0/a’ to ‘S’ based on visual inspection of more recent Pan-STARRS 1 (PS1 [Chambers et al. 2016](#)) images, SN 2008fp is updated from

‘Sa’ to ‘S0’ ([de Vaucouleurs et al. 1991](#)), SN 2012fw is updated from ‘S0/a’ to ‘S’ based on the classification of [Loveday \(1996\)](#), and PTF12jgb is updated from unclassified to ‘irregular’ based on PS1 imaging.

### 3.2.2 Host stellar mass estimates

To estimate the stellar mass of the hosts of the SNe within this sample, we used photometric measurements of the host galaxies from the Sloan Digital Sky Survey (SDSS; [Fukugita et al. 1996](#); [Gunn et al. 1998, 2006](#); [Blanton et al. 2017](#); [Doi et al. 2010](#)) and applied eqn. 8 of [Taylor et al. \(2011\)](#) as was used in [Rigault et al. \(2018\)](#). This equation provides a method of obtaining the stellar mass based on *g* and *i* band imaging and has an accuracy of  $\sim 0.1$  dex. The most appropriate magnitudes tabulated for SDSS for this analysis were found to be the Petrosian magnitudes ([Taylor et al. 2011](#)). Twenty one of the SNe Ia in our full sample have available photometry in SDSS Data Release 16 ([Ahumada et al. 2020](#)), and were obtained using the CasJobs data retrieval system. The photometry for the host of SN 2012ht was found to be unreliable due to potential blending with a coincident foreground star, and has been replaced by photometry, also in the SDSS filter system, from [Mazzei et al. \(2018\)](#). The estimated stellar masses using the method of [Rigault et al. \(2018\)](#) are given in Table 3. The mean of the log of the host stellar mass of this sample is determined to be 10.3, with a standard deviation of 0.7 dex. The log of the mean host stellar mass from the PTF sample of [Pan et al. \(2014\)](#) was 10.2 with a standard deviation of 0.8 dex, which is consistent with this sample within the uncertainties.



**Table 3.** Summary of the host galaxy mass measurements made for the hosts of the combined SNe sample using SDSS photometry.

SN	Host	$\log(M^*/M_\odot)$
SN 2006cm	UGC 11723	10.37±0.07
SN 2007af	NGC 5584	9.63±0.04
SN 2007kk	UGC 2828	11.21±0.01
SN 2007le	NGC 7721	10.26±0.01
SN 2008ec	NGC 7469	10.40±0.03
SN 2008hv	NGC 2765	10.70±0.04
SNF 20080514-002	UGC 8472	10.57±0.05
SN 2009ig	NGC 1015	10.27±0.01
SN 2010A	UGC 2019	10.15±0.01
SN 2012cg	NGC 4424	8.83±0.02
SN 2012et	CGCG 476-117	10.34±0.01
SN 2012ht	NGC 3447	8.93±0.12
LSQ12dbr	SDSS J2058-0258	7.98±0.15
PTF12iiq	(1)	10.57±0.01
SN 2013aj	NGC 5339	9.99±0.10
SN 2013U	(2)	10.34±0.05
SN 2016ipf	(3)	10.22±0.01
SN 2017hn	UGC 08204	10.59±0.31
SN 2017awz	MCG+04-26-033	10.26±0.01
SN 2017fgc	NGC 0474	10.54±0.02
SN 2017gvp	UGC 12739	10.61±0.09

\* Photometric data from [Mazzei et al. \(2018\)](#).

- (1) 2MASX J02500784-0016014
- (2) 2MASX J10011189+0019458
- (3) 2MASX J08071352+0540566

### 3.2.3 Projected distance from host nucleus

The projected distance between each SN and the centre of its host has been determined assuming that SN and host are located at the same distance and are in the same plane i.e., inclination effects are not considered. The full results of these calculations are shown in Figure 7. It is expected that ISM effects will decrease with increasing galactocentric distance making it more likely that objects at large distances showing strong blueshifted Na I D absorption are the result of CSM effects. The majority of the objects within the sample, regardless of Na I D absorption classification are found at projected distances < 12.5 kpc, though two objects (LSQ12fxd and LSQ12gdj) with blueshifted Na I D absorption are observed at larger distances (26.5 and 17.5 kpc respectively). More generally, the means for each Na I D absorption classification are found to be consistent (Blueshift: 6.5±7.2 kpc, Blue and redshift: 3.2±1.9 kpc, Non blueshift: 8.9±8.5 kpc, No absorption: 6.2±4.6 kpc) indicating no statistical relationship between Na I D absorption classification and the projected distance between SN and host nucleus.

## 3.3 Line measurements of broad SN features

One of the main aims of this paper is to determine if there is a relation between the presence of blueshifted Na I D features and the broad SN features of Si II 6355 Å and the Ca II NIR triplet seen in SNe Ia around maximum light. The typical identified broad features are shown for SN 2017fgc in Figure 6. In particular, we are interested in quantifying the presence of high-velocity components to these features with velocities 1500 km s<sup>-1</sup> higher than the photospheric contribution, which have been previously attributed to interaction with CSM (e.g., [Mazzali et al. 2005](#)). The identification of a relation would provide evidence of blueshifted Na I D features being intrinsic to the SN system and likely not coming from the ISM.

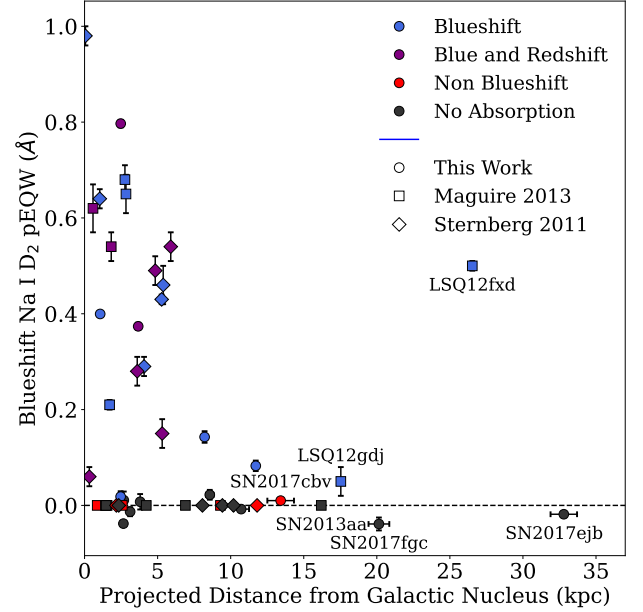


**Figure 7.** Na I D<sub>2</sub> pEQW for the full sample vs the measured projected distance between the individual SN and the nucleus of its host galaxy. SNe with projected distances exceeding 12.5 kpc are labelled.

### 3.3.1 Fitting procedure of the broad Si II and Ca II NIR features

The Si II 6355 Å and Ca II NIR triplet features were fit using Gaussian profiles broadly following the method of e.g., [Childress et al. \(2013b\)](#); [Maguire et al. \(2014\)](#). The spectra were rebinned to 1 Å resolution to increase the S/N and a sigma clipping was applied to remove any residual narrow skylines or other residual artefacts that were not corrected in the reduction process to prevent such features from influencing the fitting. The continuum was removed by selecting regions on either side of the feature and removing with a linear fit as described for the narrow Na I D features. To investigate the presence of high-velocity features in the Si II 6355 Å and Ca II NIR triplet regions, we have fitted both features under two conditions: i) the presence of only photospheric-velocity components and ii) with the additional presence of high-velocity components.

The photospheric components of the Si II feature were fit as a doublet with the relative strengths set assuming the optically thick regime ([Childress et al. 2013b](#); [Maguire et al. 2014](#)), with the full width half-maximum (FWHM) and velocity offset constrained to be the same for both doublet features. The high-velocity components of the Si II were set up in the same manner, with the high-velocity component values independent of the photospheric components. The same procedure was used for the photospheric and high-velocity components of the Ca II NIR triplet, with three linked features for each component.

The weighted mean values of the relevant fit parameters (velocity, FWHM and pEQW) were determined by varying the position of the continuum selection region and refitting 5000 times, with the uncertainties given as the standard deviation of the successful fitting parameter values, combined in quadrature with the redshift and spectral resolution uncertainty for each object. In these fits, the absorption minima velocity of the fitted high-velocity feature must exceed that of the photospheric component by at least 1500 km s<sup>-1</sup>. Based on the results of previous studies, we also make the assumption that the photospheric component is dominant and so the amplitude and width of the high-velocity component must be less

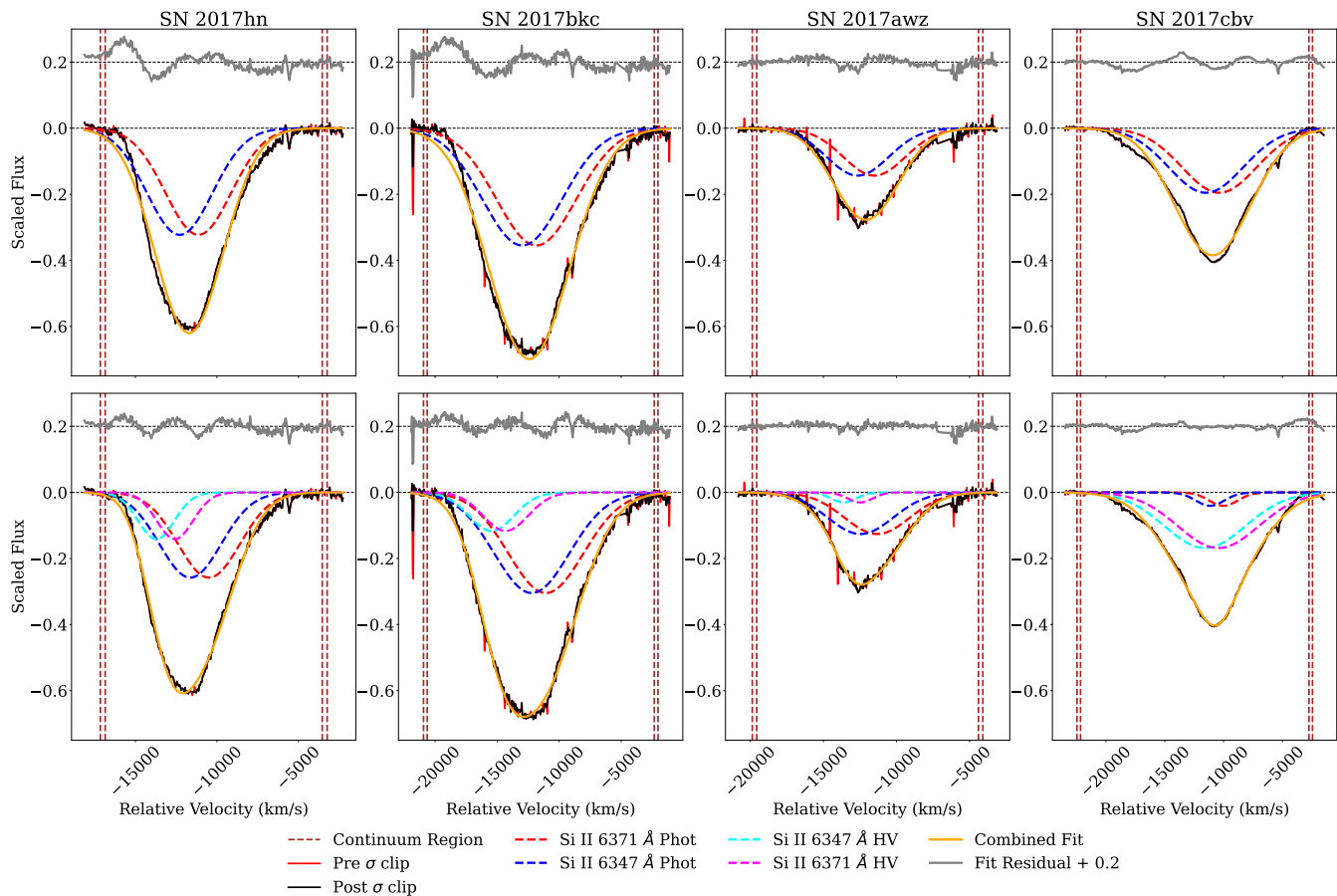


**Figure 8.** Example Si II fits for a selection of objects. Top Panels: Fitting the feature as being purely photospheric in origin. Bottom Panels: Fitting with the inclusion of a high velocity component. SNe 2017hn and 2017bkc are examples where the fit including a high velocity component reduces the overall residual pattern seen. SN 2017awz is a borderline case where including a high-velocity component provides a small overall contribution to the pEQW of the feature ( $\sim 8\%$ ) and was ultimately rejected due to no fitting iteration reaching the required component separation (absorption minima velocities differ by  $\sim 1200$   $\text{km s}^{-1}$ ). The fitting of SN 2017cbv is considered to have failed given the very broad nature of the high velocity component, the large high-velocity pEQW contribution ( $\sim 88\%$ ) and the small velocity separation between the photospheric and high-velocity components ( $\sim 600$   $\text{km s}^{-1}$ ).

than those of the photospheric component. Additionally the widths of both components must exceed  $1000$   $\text{km s}^{-1}$  to disallow any fits where a narrow noise feature within spectrum has dominated the results. The Ca II NIR triplet spectral region is less clean than the Si II  $6355$  Å region, with a potential contribution from the O I  $8446$  Å feature. We have performed tests including this potential contribution but do not obtain reliable results. Therefore, the O I  $8446$  Å feature is not included in our fitting. To ensure consistency of results, the spectra forming the combined dataset of Maguire et al. (2013) and Sternberg et al. (2011) have also been fitted using this method where the necessary data are available. These results are presented in Tables A1 and A2 for the Si II and Ca II NIR features, respectively, for the Maguire et al. (2013) sample and in Tables A3 and A4 for Si II and Ca II NIR features, respectively, for the Sternberg et al. (2011) sample.

### 3.3.2 Determination of the presence of high-velocity components

The presence of a high-velocity Si II feature is determined by the comparison of the fits with and without a high-velocity component using the Bayesian information criterion (BIC, Schwarz

1978), where the inclusion of a high-velocity component is strongly favoured if  $\Delta\text{BIC} > 10$ . Additionally, the fitting of a high-velocity feature must be successful in at least 500 iterations (at least 10 % of iterations) to prevent the comparisons being unduly weighted by a small number of outlying fits.

The results of the fits for the Si II feature are shown in Table 4, with example fits shown in Fig 8. Three SNe Ia (SNe 2017awz, 2017azw, 2017cbv) in the sample do not require the inclusion of high-velocity Si II component and are well fit using a photospheric component alone. All remaining objects satisfy the requirements for a high-velocity component based on the BIC and on the number of successful fitting iterations. In a similar manner, the presence of a high-velocity Ca II was also determined using the same constraints on BIC and number of successful fitting iterations (Table 5). Figure 9 showing example fits to several objects within the sample. A Ca II feature was not observed in SN 2016hvl, likely due to its early phase ( $-8$  d) and 91T-like classification. All of the remaining 14 objects satisfy the selection criteria and are thus identified as displaying high-velocity Ca II absorption.

**Table 4.** Summarised fitting results for the Si II 6355 Å feature. Means have been weighted using the relevant fitting uncertainties with the uncertainties of these means obtained as the standard deviation of the results. A positive value of  $\Delta\text{BIC}$  indicates a preference for the inclusion of a high velocity feature based on statistical considerations alone.

No High Velocity component								
SN	Photospheric Component			High Velocity Component			$\chi^2$	$\Delta\text{BIC}$
	Min V (km s <sup>-1</sup> )	FWHM (km s <sup>-1</sup> )	pEQW (Å)	Min V (km s <sup>-1</sup> )	FWHM (km s <sup>-1</sup> )	pEQW (Å)		
SN 2017awz	-11520 ± 50	4970 ± 60	31.0 ± 0.2	-	-	-	0.075 ± 0.003	*
SN 2017azw	-11820 ± 110	6510 ± 70	69.6 ± 0.5	-	-	-	0.121 ± 0.015	*
SN 2017cbv	-10370 ± 110	7450 ± 50	63.5 ± 0.2	-	-	-	0.097 ± 0.001	*
Mean	-11320 ± 630	6370 ± 1020	53.1 ± 16.9	-	-	-	0.094 ± 0.019	-
With High Velocity component								
SN	Photospheric Component			High Velocity Component			$\chi^2$	$\Delta\text{BIC}$
	Min V (km s <sup>-1</sup> )	FWHM (km s <sup>-1</sup> )	pEQW (Å)	Min V (km s <sup>-1</sup> )	FWHM (km s <sup>-1</sup> )	pEQW (Å)		
SN 2016hvl	-7950 ± 200	11950 ± 350	16.9 ± 0.2	-12450 ± 80	4100 ± 130	2.9 ± 0.2	0.100 ± 0.001	120 ± 50
SN 2016ipf	-9740 ± 100	8030 ± 220	93.4 ± 3.2	-13340 ± 820	6350 ± 1270	15.8 ± 3.2	0.215 ± 0.027	100 ± 90
SN 2017hm	-9720 ± 260	5830 ± 200	75.4 ± 7.2	-12410 ± 130	3280 ± 450	17.3 ± 7.2	0.052 ± 0.007	630 ± 80
SN 2017hn	-10470 ± 120	4450 ± 60	49.6 ± 1.3	-12560 ± 120	2650 ± 120	16.6 ± 1.3	0.122 ± 0.006	330 ± 50
SN 2017yv	-11470 ± 90	6930 ± 210	97.6 ± 3.1	-14290 ± 540	3730 ± 1070	10.9 ± 3.1	0.189 ± 0.073	280 ± 200
SN 2017bkc	-11110 ± 80	6960 ± 100	94.6 ± 1.7	-14460 ± 100	3980 ± 170	19.9 ± 1.7	0.201 ± 0.016	400 ± 30
SN 2017ckq	-9880 ± 190	5960 ± 120	76.2 ± 4.9	-12110 ± 70	2630 ± 410	8.9 ± 4.9	0.038 ± 0.006	680 ± 100
SN 2017ejb	-9070 ± 170	7550 ± 60	88.1 ± 3.3	-11520 ± 110	3340 ± 240	15.2 ± 3.3	0.088 ± 0.030	760 ± 100
SN 2017fgc	-13940 ± 140	9120 ± 100	118.6 ± 2.4	-18870 ± 120	5420 ± 120	32.5 ± 2.4	0.132 ± 0.004	940 ± 40
SN 2017fzw	-12190 ± 120	8660 ± 90	123.4 ± 1.5	-17460 ± 110	5140 ± 70	48.6 ± 1.5	0.234 ± 0.008	1030 ± 40
SN 2017gah	-12100 ± 190	10130 ± 260	141.6 ± 5.7	-15240 ± 820	6120 ± 1910	18.4 ± 5.7	1.744 ± 0.355	120 ± 100
SN 2017gvp	-10680 ± 50	7100 ± 60	86.2 ± 0.7	-12520 ± 60	3420 ± 100	9.8 ± 0.7	0.082 ± 0.000	400 ± 60
Mean	-10700 ± 1530	7080 ± 1950	66.7 ± 31.4	-13490 ± 2160	3770 ± 1290	8.7 ± 11.7	0.091 ± 0.466	520 ± 310

\* No  $\Delta\text{BIC}$  values are available for these objects as all fitting iterations when including a high-velocity feature were unsuccessful.

**Table 5.** Summarised fitting results for the Ca II NIR triplet feature. Means have been weighted using the relevant fitting uncertainties with the uncertainties of these means obtained as the standard deviation of the results. A positive value of  $\Delta\text{BIC}$  indicates a preference for the inclusion of a high velocity feature based on statistical considerations alone.

No High Velocity component								
SN	Photospheric Component			High Velocity Component			$\chi^2$	$\Delta\text{BIC}$
	Min V (km s <sup>-1</sup> )	FWHM (km s <sup>-1</sup> )	pEQW (Å)	Min V (km s <sup>-1</sup> )	FWHM (km s <sup>-1</sup> )	pEQW (Å)		
SN 2016ipf	-9060 ± 40	7620 ± 40	86.4 ± 0.2	-17890 ± 40	5420 ± 40	31.8 ± 0.2	0.588 ± 0.003	560 ± 70
SN 2017hm	-9730 ± 40	5470 ± 30	114.4 ± 0.1	-18580 ± 40	6140 ± 30	87.5 ± 0.1	0.609 ± 0.003	1500 ± 50
SN 2017hn*	-10790 ± 110	4650 ± 40	114.2 ± 0.1	-18720 ± 110	5300 ± 40	58 ± 0.2	1.360 ± 0.006	1130 ± 50
SN 2017yv	-10980 ± 40	6350 ± 40	126.7 ± 0.1	-17590 ± 40	5420 ± 40	33.6 ± 0.2	0.574 ± 0.004	490 ± 50
SN 2017awz	-11360 ± 40	3180 ± 40	19.3 ± 0	-17460 ± 40	3690 ± 40	8.9 ± 0.1	0.107 ± 0.002	710 ± 70
SN 2017azw*	-11230 ± 110	3090 ± 30	41.6 ± 0.6	-22060 ± 110	6300 ± 40	97.9 ± 0.1	1.582 ± 0.005	1120 ± 60
SN 2017bkc	-10790 ± 40	7380 ± 40	152.4 ± 0.6	-15380 ± 40	5050 ± 40	60.3 ± 0.6	0.398 ± 0.003	310 ± 60
SN 2017cbv*	-9360 ± 110	3960 ± 50	34.5 ± 0.3	-19370 ± 110	5420 ± 40	84 ± 0.2	0.480 ± 0.003	1440 ± 60
SN 2017ckq*	-9690 ± 40	5030 ± 30	96.2 ± 0.1	-16730 ± 40	2810 ± 40	19.1 ± 0	0.552 ± 0.002	830 ± 50
SN 2017ejb*	-8670 ± 110	7180 ± 40	137.7 ± 0.4	-13450 ± 110	4620 ± 30	118.4 ± 0.4	1.546 ± 0.008	580 ± 50
SN 2017fgc	-12150 ± 110	6340 ± 40	102.6 ± 1.1	-18670 ± 110	7710 ± 50	168.4 ± 1.2	0.368 ± 0.009	850 ± 60
SN 2017fzw	-10330 ± 110	6570 ± 40	123.5 ± 0.6	-17750 ± 110	7370 ± 40	184.3 ± 0.7	0.807 ± 0.016	1090 ± 60
SN 2017gah*	-8560 ± 110	6090 ± 40	117.5 ± 0.3	-15790 ± 110	7140 ± 40	174.4 ± 0.4	1.125 ± 0.011	900 ± 60
SN 2017gvp	-10120 ± 40	4970 ± 40	78.7 ± 0.1	-19860 ± 40	6120 ± 40	74.7 ± 0.1	0.462 ± 0.003	1540 ± 50
Mean	-10210 ± 1040	5540 ± 1430	76.6 ± 38.6	-17730 ± 2020	5540 ± 1310	57.9 ± 55.5	0.621 ± 0.447	950 ± 370

\* Residual pattern indicative of the presence of an additional feature

## 4 RESULTS

The following section first outlines the results of the analysis conducted of the broad SN features and the narrow Na I D absorption features. It then describes the connection between the host galaxy properties and the Na I D features, as well as quantifying the observed excess of blueshifted Na I D absorption features. Following this, results of comparisons between the light curve properties and Si II features to the classification of Na I D features are described, before exploring similar comparisons with the properties of the Ca II feature.

### 4.1 Broad SN features and the presence of high-velocity components

Fitting of the broad Si II 6635 Å features found that three of the 15 objects (20 %) in the new sample were well described using a purely photospheric feature, with the rest being better fit with the inclusion of a high-velocity component (Table 4). The mean photospheric components (velocity, pEQW, FWHM) of the sub-sample with and without a high-velocity are found to be consistent within the uncertainties. The fitting of the broad Ca II NIR triplet absorption feature was found to heavily favour the inclusion of a

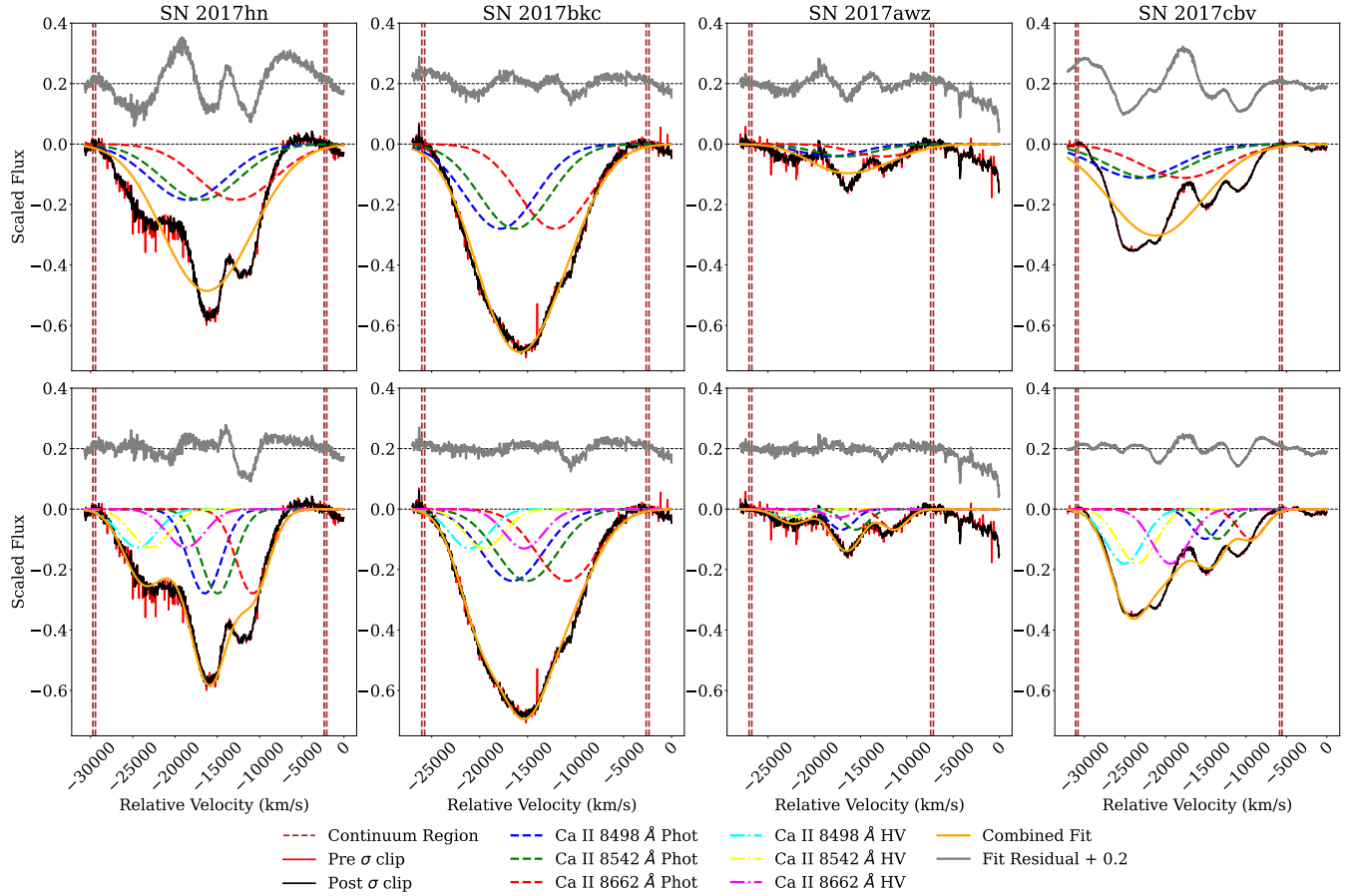


**Figure 9.** Example Ca II fits for a four SNe Ia. Top panels: Fitting the feature as being purely photospheric in origin. Bottom Panels: Fitting with the inclusion of a high-velocity component. The fitting for all four objects prefer the inclusion of a high-velocity component. However, the features of SNe 2017hn and 2017cbv retain residual patterns indicative of other contributing features e.g., O I that are not accounted for even with the inclusion of the high velocity Ca II.

high-velocity feature, with all 14 objects for which it was possible to fit the Ca II NIR triplet region found to be better described with the inclusion of a high-velocity component. The values measured for the fits are given in Table 5. The velocities measured for the Si II and Ca II photospheric components are found to be consistent within the uncertainties. However, values given in Table 5 show that the high-velocity components of the Si II features are narrower and lower velocity than those measured for the Ca II NIR triplet.

## 4.2 Na I D equivalent widths

As outlined in Section 3.1.2, measurements of the strength for the Na I D features have been made, using the stronger of the two lines (Na I D<sub>2</sub>) as a proxy for overall strength. Previous studies have suggested that those SNe Ia showing blueshifted Na I D absorption have a tendency to display stronger overall Na I D absorption features (higher pEQW) compared to the rest of the population (Phillips et al. 2013).

When those SNe Ia showing ‘no absorption’ and the ‘blue and redshifted’ absorption are removed from the comparison in the full sample, the remaining objects (i.e. those showing ‘only blueshifted’ or ‘non blueshifted’ Na I D absorption) are well described by a single pEQW distribution. Whilst the median values for the blueshifted and non-blueshifted groups are rather different (0.64 and 0.24 respec-

tively), the corresponding mean values are found to be consistent at  $0.46 \pm 0.34 \text{ \AA}$  and  $0.40 \pm 0.39 \text{ \AA}$  respectively, additionally a K-S test indicates that the two groups are drawn from the same overall population (K-S statistic: 0.333, p-value: 0.657). We note that the non-blueshifted Na I D sub-sample is small with only six objects but we do not identify any clear difference between them. This result is shown in Figure 10. As would be expected, this plot also shows that objects showing blue and redshifted Na I D absorption tend to have stronger overall absorption features, which is unsurprising since these objects have multiple absorption components. The pEQWs of the blueshifted components of objects with both blue and redshifted Na I D absorption features are of comparable strength to those of objects showing purely blueshifted Na I D absorption.

## 4.3 Host galaxy distribution and connection to narrow Na I D absorption features

Previous studies have shown that SNe Ia with late-type host galaxies (spiral galaxies) typically have brighter absolute magnitudes and broader light curves (larger ‘stretch’ values), compared to those hosted by early-type galaxies (elliptical and lenticular galaxies), which have been seen to host intrinsically fainter and faster evolving events (Hamuy et al. 1995, 1996, 2000; Riess et al. 1999). It has also been observed that SNe Ia occurring in late-type galaxies have

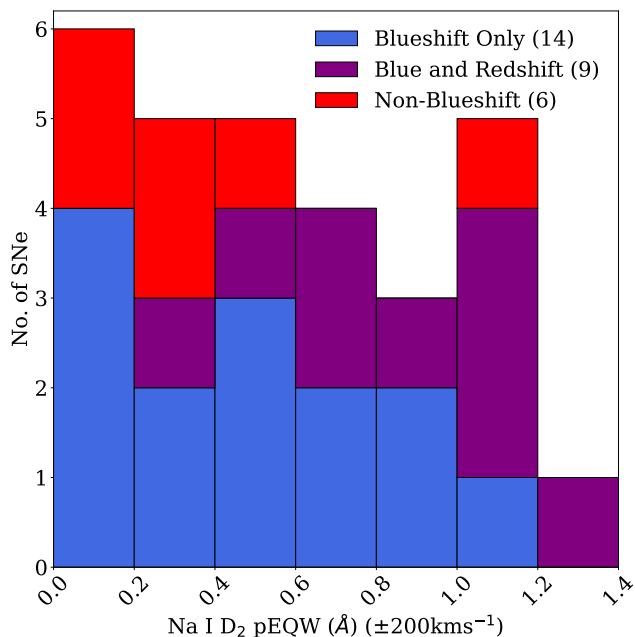


**Figure 10.** Distribution plots for the measured full feature Na I D<sub>2</sub> pEQWs. Those objects showing no Na I D absorption features are not included. We find no statistical difference in the pEQW of the blueshifted only and non-blueshift sub-samples.

a higher incidence of blueshifted Na I D absorption features compared to those in early-type galaxies which are more likely to show no Na I D absorption features (Sternberg et al. 2011; Maguire et al. 2013). The sample of new SNe Ia in this work confirms this previously observed trend with all six of the SNe with blueshifted Na I D absorption features associated with late-type spiral hosts, compared to just two of the SNe Ia showing no or non-blueshifted Na I D absorption features (left panel of Figure 11). The full combined sample of objects also shows a similar distribution (right panel of Fig 11).

Figure 12 provides a comparison between the blueshifted Na I D EQW and the measured host stellar masses of the full sample. Given the reduced number of objects with available host mass estimates, no clear distinctions between the different sub-samples based on Na I D EQW can be identified, with the log mean host stellar masses of the sub-samples being consistent,  $9.93 \pm 0.59 M_{\odot}$  (‘blue and redshifted’),  $10.29 \pm 0.13 M_{\odot}$  (‘blueshifted only’),  $10.36 \pm 0.94 M_{\odot}$  (‘no absorption’), with a mean of  $10.31 \pm 0.72 M_{\odot}$  for the full sample.

#### 4.4 Observed excess of blueshifted Na I D features

As previously described, for Na I D features produced by absorbing material within the host galaxy of the SN but not related to the SN itself, it would be expected that an equal number of SNe would display unrelated blueshifted and redshifted Na I D absorption features, as there is no physical reason why material along the same line of sight would have a location bias in front (producing blueshifted features) or behind (producing redshifted features) of a particular SN (but see Hoang 2017). However, previous studies (Sternberg et al. 2011; Maguire et al. 2013) have identified an excess of blueshifted compared to redshifted Na I D components in SN Ia samples. Using

**Table 6.** Summary of the Na I D feature classifications of the SN Ia samples and the corresponding %EB values.

Na I D Classification	Number of Events	
	This Work’s Sample	Combined Sample
Blueshifted only	4	14
Redshifted only	1	5
Symmetric	0	1
No Absorption	8	18
<b>Total Included</b>	<b>13</b>	<b>38</b>
<b>%EB<sup>a</sup></b>	<b>23</b>	<b>24</b>
<b>Excluded</b>		
Blue and Redshifted	2	9
<b>Full Object Total</b>	<b>15</b>	<b>47</b>

<sup>a</sup> The calculation used to determine the percentage excess of blueshifted Na I D features observed is detailed in Section 4.4.

our new sample of 15 SNe Ia, we have calculated the percentage excess of blueshifted Na I D features (%EB) using,

$$\%EB = \left( \frac{B - R}{B + R + N + S} \right) \times 100 \quad (1)$$

where B and R are the numbers of events showing exclusively blue and redshifted features respectively, N is the number of events with no observed Na I D absorption features, and S represents the objects displaying a symmetric absorption profile around  $0 \text{ km s}^{-1}$ . This is similar to the method of Maguire et al. (2013) but for this calculation, any object that displays a combination of red and blueshifted features was excluded given that identifying the source of these features is problematic. Maguire et al. (2013) excluded such events from the counts of events showing red or blueshifted features but not from the total number of objects. This exclusion fully removes objects that may have narrow Na I D absorption features from different sources (e.g., CSM and host galaxy ISM contamination), which could affect the statistical calculations.

For the new sample of SNe Ia in this work, %EB is found to be 23 %, while the full sample has an %EB value of 24 %. A summary of the classifications of the objects included in the new and full samples is given Table 6. If the probability of a given SN displaying blue- or red-shifted Na I D features is taken to be equal, as would be expected through purely line-of-sight/host-galaxy contamination, the cumulative binomial probability of observing at least 14 events with blueshifted only Na I D features compared to five showing purely redshifted Na I D features is approximately 3.1 per cent.

It is expected that SNe in late-type galaxies show Na I D absorption features more commonly as a consequence of their more gas rich host environments relative to early-type galaxies (with the specifics dependent on the specific local environment of each SN) resulting in additional contamination from unrelated material on coincidental lines of sight to the SN. There is, however, no environmental process that should favour the generation of blue or redshifted features relative to the SN rest frame. To explore this further, %EB was also calculated separately for those objects with hosts classified as early-type (E and S0) and those with late-type (S), with those hosted by dwarf or irregular galaxies being excluded. Like the previous calculations, objects showing both red and blueshifted features are also excluded. A clear difference between the observed %EB in early- and late-type galaxies is seen (Table 7). For early-type galaxies, the negative %EB (−8 per cent) indicates that fewer



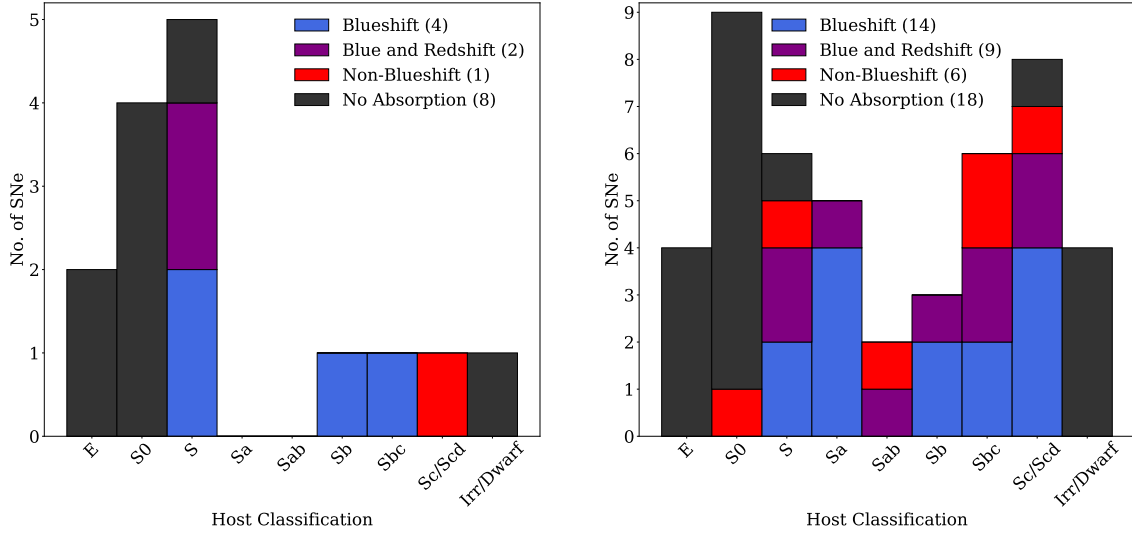


**Figure 11.** Left panel: Host galaxy morphological distribution of the new SNe Ia sample discussed in this work. Objects have been divided based on the classification of the Na I D feature. Right panel: Host galaxy distribution of the combined SNe Ia sample.

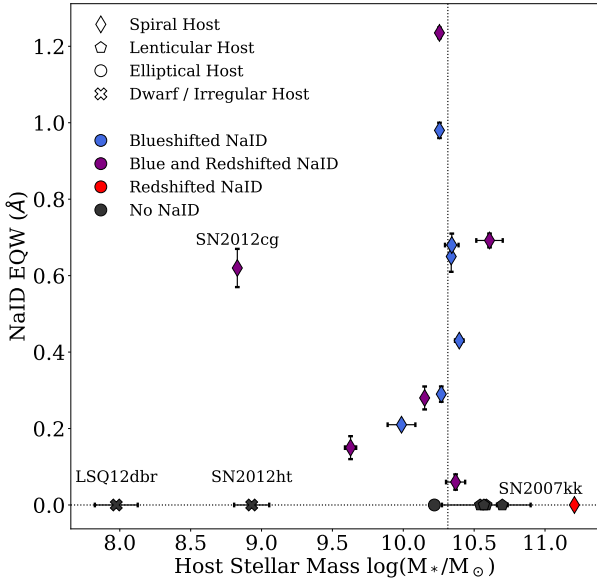


**Figure 12.** Blueshifted Na I D EQW against host stellar mass. Overall sample mean mass ( $10.31 \pm 0.71$ ) is indicated by the dashed vertical line. The three lowest mass and the highest mass hosts are labelled. The morphological types are also listed in the legend, along with the Na I D classifications.

objects with blueshifted Na I D features have been observed than would be expected from an even split in distribution. This negative value is likely a result of the small sample size since there are no known processes that favour an overproduction of redshifted narrow Na I D absorption. Indeed this value is produced by the one detection of a purely redshifted feature in SN 2008fp, further highlighting that early-type galaxies with no absorption features (12 of 13 in this sample) appear to be the norm. In contrast, the %EB calculated for the SNe Ia in late-type galaxies shows a strong excess of observed blueshifted features (48 per cent). A corresponding increase in SNe Ia with redshifted Na I D features is not seen in the late-type host galaxies, as would be expected from isolated ISM contribu-

**Table 7.** Summary of the Na I D feature classifications of the combined SNe Ia sample sub-divided by host galaxy classification and the corresponding %EB values.

Na I D Classification	Number of Events	
	Early-Type Only	Late-Type Only
Blueshifted only	0	14
Redshifted only	1	4
Symmetric	0	1
No Absorption	12	2
<b>Total Included</b>	<b>13</b>	<b>21</b>
<b>%EB<sup>a</sup></b>	<b>-8</b>	<b>48</b>
<b>Excluded</b>		
Blue and Redshifted	0	9
<b>Full Object Total</b>	<b>13</b>	<b>30</b>

tions alone. The cumulative binomial probability of obtaining this distribution through random chance is approximately 1.5 per cent.

#### 4.5 Light curve properties and Si II velocities compared to Na I D absorption shifts

In this section, we investigate the connection between light curve width and  $B-V$  colour at maximum and the Na I D absorption classifications. The stretch distribution of this new sample alone and the full sample are shown in the left and right panels of Figure 13, respectively. A K-S test was conducted on the full sample, comparing the measured stretch values of the SNe showing any blueshifted Na I D component to those showing non-blueshifted or no such features, with the resulting K-S statistic of 0.393 and a p-value of 0.047 indicating that there is a statistically significant difference between the two groups. This is in agreement with the results of Foley et al. (2012) and Maguire et al. (2013) where it was observed that SNe Ia showing no Na I D absorption features have faster evolving light curves (lower stretch values) than those showing any Na I D absorption. When the light curve stretch values of the full sample are divided into four corresponding to their Na I D classification, the

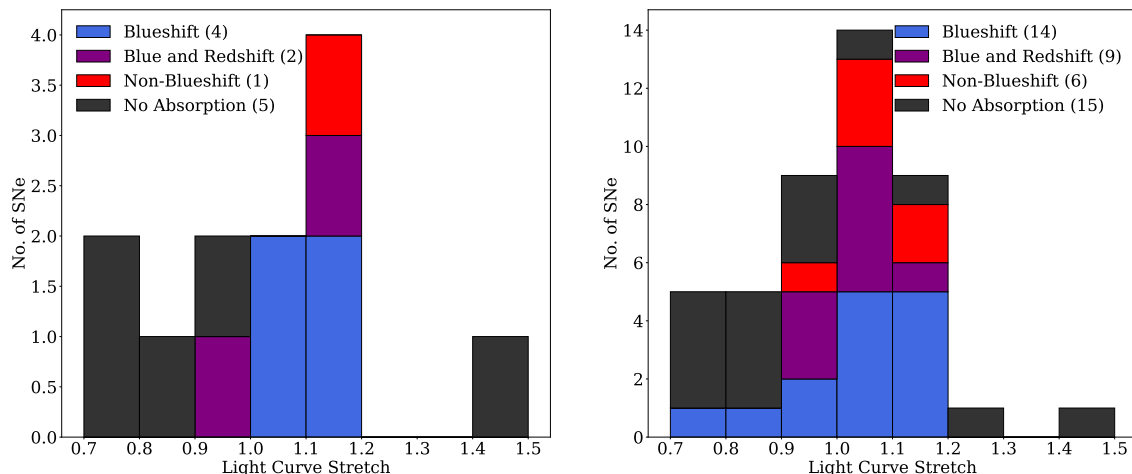


**Figure 13.** Left panel: Stretch distribution plot of the new SNe Ia sample discussed in this work. Right panel: Stretch distribution plot of the ‘full’ SNe Ia sample. The sample is divided based on the properties of their narrow Na I D features.

weighted mean stretch values are measured to be  $1.02 \pm 0.11$ ,  $1.03 \pm 0.08$ ,  $1.06 \pm 0.05$  and  $0.86 \pm 0.20$  for blueshifted only, blue and redshifted, non-blueshifted, and no Na I D absorption, respectively. The average light curve stretch value for those SNe Ia showing no Na I D absorption features is smaller than the other classifications but they are all marginally consistent within the uncertainties. In agreement with Maguire et al. (2013), we do not identify any relation between the strength (as described by the pEQW) of the blueshifted Na I D absorption feature of a given SN and its light curve stretch.

The relationship between light curve width and Na I D absorption classification is associated with the host distribution of the SNe Ia within these samples, as those SNe with no Na I D absorption features largely occur in early-type galaxies, which as discussed in Section 4.3 are known to host less luminous and faster evolving SNe Ia. Two of the four SNe Ia with broad light curves (stretch values exceeding one) and showing no Na I D absorption (LSQ12dbr and PTF12jgb) occurred within irregular galaxies (that can have histories of recent star formation), with a third (SN 2017hn) hosted by an S0 galaxy, highlighting that the true relationship is more than a simple early/late-type host galaxy split.

Previous studies have identified a relation between  $B-V$  colour at maximum light and the strength of any blueshifted Na I D absorption features (Foley et al. 2012; Maguire et al. 2013). A similar investigation of the full sample has been conducted here (Figure 14) though we fit the those objects showing purely blueshifted Na I D absorption separately from those showing both blue and redshifted Na I D absorption. This analysis reveals the previously found result that SNe Ia with stronger blueshifted Na I D absorption features (higher pEQWs) display larger  $B-V$  values (i.e., redder colours) is present only for objects showing purely blueshifted Na I D absorption with no such trend observed for objects displaying blue and redshifted absorption. The fitted relation between  $B-V$  colour at maximum and the pEQW of the blueshifted Na I D<sub>2</sub> Na I D for those objects classified as showing ‘blueshifted’ Na I D absorption retrieves the correlation at  $5.2\text{-}\sigma$  significance (provided by the ODR fitting routine). We discuss the possible origin of this correlation further in Section 5.3.

We also explored if there was a correlation between the measured velocity of the Si II features and Na I D pEQW. The full sample confirms the result of Maguire et al. (2013) that no such correla-

tion is observed for either the photospheric or high velocity (where present) Si II features.

#### 4.6 Ca II absorption properties compared to Na I D absorption, light curve ‘stretch’ and SN colour

Previous studies (e.g., Mazzali et al. 2005; Childress et al. 2013a; Maguire et al. 2014), have shown that high-velocity components of the Ca II NIR absorption features of SNe Ia obtained near the time of maximum light are very common. There are previous suggestions that they could be due to CSM (Gerardy et al. 2004; Mazzali et al. 2005; Quimby et al. 2006; Tanaka et al. 2008) or may be intrinsic to the SN itself (Branch et al. 2006; Blondin et al. 2012). Here we have found that 14 of the 15 objects for which we could obtain measurements display such features (93 per cent). The non-detection in one event (SN 2016hvl) is likely due to a combination of its early phase ( $\sim 8$  d prior to maximum light) along with its classification as a 91T-like event, which typically show weaker absorption features from intermediate-mass elements. As the high-velocity Ca II absorption features are so common, it is impossible to link the simple occurrence of such features to the properties of any Na I D absorption features, blueshifted or otherwise. Therefore, to examine any potential link between the strength of blueshifted Na I D absorption and high velocity Ca II features, the detailed properties of the Ca II features must be examined.

Following the method of Childress et al. (2013a), the strength of the Ca II high velocity features is characterised through the ratio of the pEQWs of the high- to photospheric-velocity components (Ca II  $R_{\text{HVF}}$ ), with objects having a ratio exceeding one defined as those showing ‘strong’ high velocity Ca II. In the interpretation that high-velocity Ca II features come from the same CSM that may be responsible for the blueshifted narrow Na I D features, then a connection between the Ca II  $R_{\text{HVF}}$  around peak and the pEQW of the blueshifted narrow Na I D features should be seen, with SNe Ia with the strongest high velocity Ca II features also showing the highest blueshifted Na I D<sub>2</sub> pEQWs. We show this comparison for our full sample in the upper left panel of Figure 15 but identify no trend between the strength of narrow blueshifted Na I D absorption and the strength of the Ca II  $R_{\text{HVF}}$ , with those SNe Ia classified as showing blueshifted Na I D<sub>2</sub> absorption features having a wide range of Ca II  $R_{\text{HVF}}$ . There are also a number of SNe Ia in the

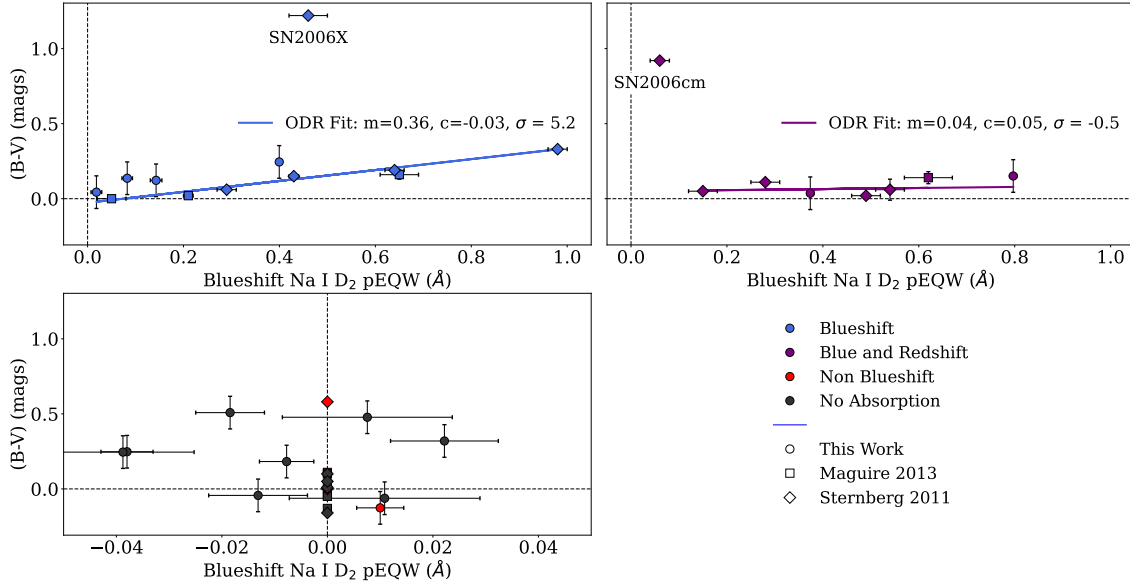


**Figure 14.**  $B-V$  colour against the blueshifted Na I D<sub>2</sub> pEQW for the full sample. Top left panel: Objects displaying purely blueshifted Na I D absorption the ODR line of best fit to these points (excluding the extreme outlier SN 2006X) is also shown (solid blue line). Top right panel: Objects displaying blue and redshifted Na I D absorption the ODR line of best fit to these points excluding the extreme outlier SN 2006cm which like SN 2006X is known to be highly reddened) is also shown (solid purple line) - no trend is identified. Bottom panel: Objects showing no, or non blueshifted Na I D absorption. In all panels the dashed black lines mark the position of zero  $B-V$  colour and zero blueshifted Na I D absorption.

sample with no Na I D absorption that display Ca II  $R_{HVF}$  values about one, which is difficult to explain in scenario where both of these probes suggest interaction with CSM.

We have also investigated any potential link between the Ca II  $R_{HVF}$  and the light curve stretch,  $B-V$  colour at maximum, and the stellar mass of the host galaxy for the sample. Previous studies (Childress et al. 2013a; Maguire et al. 2013) identified a relation between light curve width and Ca II  $R_{HVF}$  ratio, with SNe Ia with high Ca II  $R_{HVF}$  ratios also having broader light curves. We do not see this trend for our sample, with a significant fraction of SNe Ia with high Ca II  $R_{HVF}$  ratios having narrow light curves (upper right panel of Figure 15). There is a preference for SNe Ia with blueshifted Na I D to have broad light curves than the rest of the sample but as discussed in Section 4.3, this may be driven by the preference for SNe Ia with blueshifted Na I D features for late-type host galaxies, which produce more SNe Ia with broad light curves. Similarly to Childress et al. (2013a), we do not observe a correlation between Ca II  $R_{HVF}$  ratio and  $B-V$  colour at maximum (bottom left panel of Figure 15). Pan et al. (2014) identified that SNe Ia with high Ca II  $R_{HVF}$  ratios are preferentially found in low-mass galaxies. Our sample size is small so we can not draw any strong conclusion from our data on this connection (bottom right panel of Figure 15).

## 5 DISCUSSION

In this paper, we have presented a new sample of 15 SNe Ia with medium-resolution X-shooter spectra, where the properties of narrow Na I D features were studied. We have investigated the connection between the presence of narrow Na I D features, broad SN spectral features (in particular high-velocity features), light curve properties, and the host galaxy stellar mass in a full sample of 47 SNe Ia (including literature events). Now, we further discuss the implications of these results for our understanding of SNe Ia and their progenitors.

### 5.1 Confirmation of an excess of blueshifted Na I D in late-type hosts

The statistical analysis of Na I D absorption shows a strong preference for displaying the feature blueshifted, with an excess of 23 per cent in the new sample and an overall 24 per cent excess in the full sample. These values are consistent with previous results of a lower limit of  $\sim 20$  per cent in spiral hosts showing an excess (Sternberg et al. 2011; Maguire et al. 2013). As was also seen in these previous studies, the SNe Ia displaying these blueshifted features are strongly concentrated in late-type host galaxies (Figs. 11 and 12). Late-type galaxies in general contain more gas and dust than early-type galaxies (e.g., Galliano et al. 2018), thus it is expected that more SNe occurring within late-type galaxies would have spectra showing Na I D absorption features (both blue and redshifted relative to the zero velocity position of the SN). As such, a population of SNe Ia occurring within late-type galaxies would be expected to show more narrow absorption features than a population of SNe located in early-type galaxies, even if the properties of the underlying SNe were obtained from the same distribution. However, there is no reason for such a population to have a preference for blueshifted over redshifted Na I D features.

We have found that the small sample of SNe Ia hosted by irregular or dwarf galaxies (four events) showed no Na I D absorption features. Irregular galaxies tend to have young stellar populations and display star formation rates comparable to, though with a greater variance, than late-type galaxies, as well as having higher dust contents (Hunter 1997; Hunter et al. 2006). While the sample is small, the apparent difference in the Na I D absorption behaviour of these objects warrants additional study to determine if it is significant and its origin. One difference between these populations would be the lower metallicities of irregular/dwarf galaxies compared to spiral galaxies (Grebel 2004), although why this would result in different Na I D strengths is unclear.

We have confirmed the previous result of Foley et al. (2012)

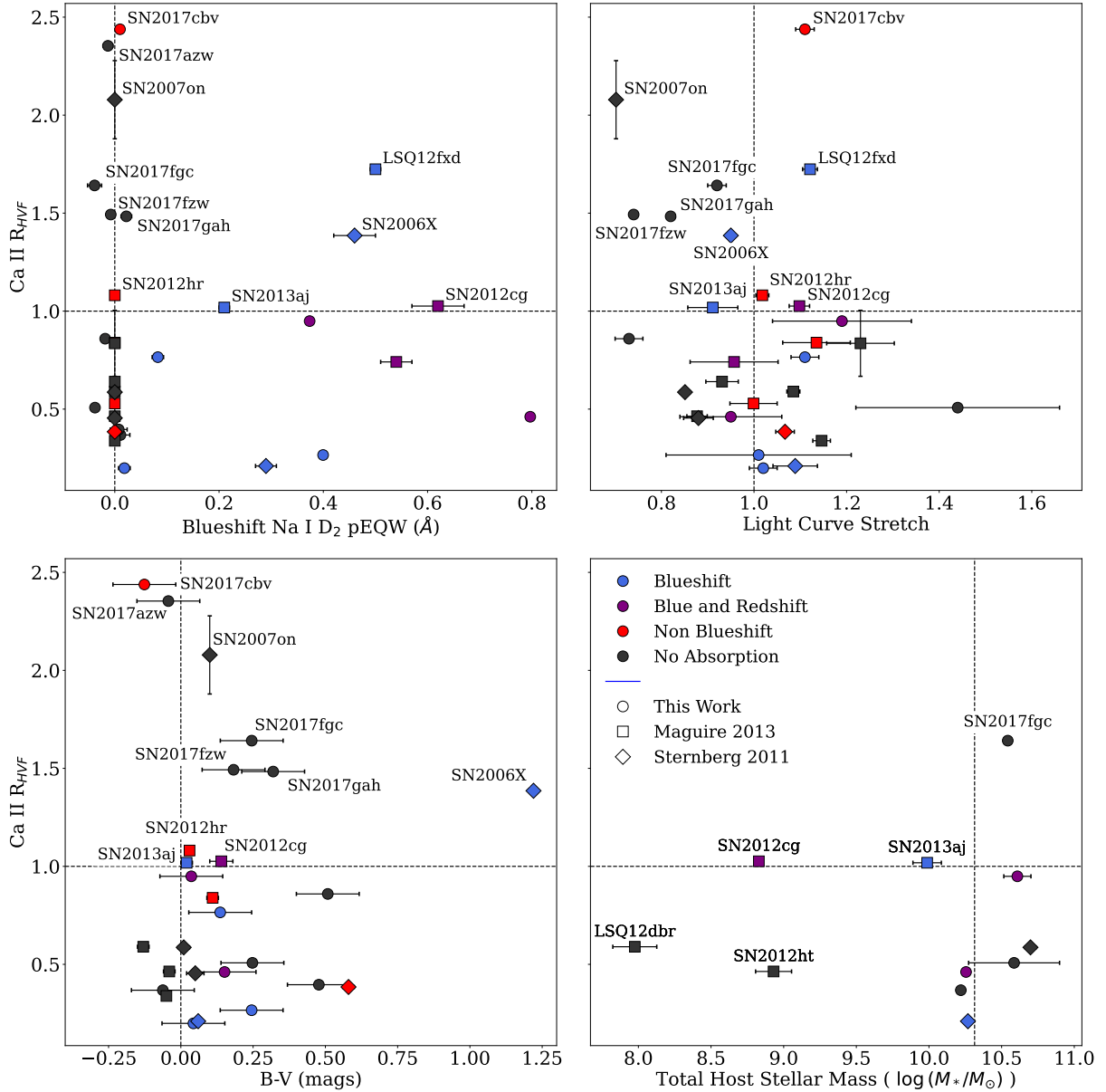


**Figure 15.** In all panels, the dashed horizontal line indicates the divide between those objects showing strong HV Ca II ( $>1$ ) and the remainder of the sample. The sample is broken down into the original source and type of Na I D shift as shown in the legend. Upper left panel: Comparison between the Ca II  $R_{HVF}$  ratio and Na I D<sub>2</sub> pEQW measurements for our full sample. The dashed vertical line at Na I D absorption strength of zero is present to guide the eye. Upper right panel: Comparison between the Ca II  $R_{HVF}$  ratio and light curve stretch. The dashed vertical line at stretch = 1 is present to guide the eye. Lower left panel: Comparison between the Ca II  $R_{HVF}$  ratio and SN  $B-V$  colour at maximum. The dashed vertical line at  $B-V = 0$  loosely divides the sample into blue and red objects. Lower right panel: Comparison between the Ca II  $R_{HVF}$  ratio and the measured total host galaxy mass of each object where available. The dashed vertical line in this panel marks the mean mass of the sample.

and Maguire et al. (2012) that SNe Ia with broader light curves are also more likely to display Na I D than those with narrower light curves (Figure 13). There is a well-known trend that late-type galaxies preferentially host brighter (broader light curve) SNe Ia (e.g., Sullivan et al. 2010) so the result that both the galaxy type and the SN light-curve width correlate with the presence of blueshifted Na I D is unsurprising. However, it is unclear what is the driving force behind this correlation. Is it that brighter SNe Ia with broader light curves that occur in late-time hosts intrinsically show preferentially blueshifted Na I D absorption or is this an age or metallicity

effect? Do SNe Ia in spiral galaxies have a different progenitor population to those in early-type host galaxies?

## 5.2 Lack of a link between blueshifted Na I D and high-velocity Ca II features

In the previous section, we discussed how SNe Ia with blueshifted Na I D have broader light curves but this may be driven by their preference for late-type host galaxies and their differing environments. One of the main aims of this study was to investigate, for the first time, if there is a connection between the presence of broad

high-velocity Ca II features in SNe Ia and the presence of narrow blueshifted Na I D features. As previously discussed, high-velocity Ca II features are ubiquitous in SNe Ia and we confirm this here finding that the vast majority of the sample require a high-velocity Ca II component. We also identify high-velocity Si II features in 12 SNe Ia in our sample, although these features are not clearly ‘detached’ from the photospheric component. The reason that high-velocity features are interesting to investigate in connection with blueshifted Na I D features is that there are suggestions that the high-velocity Ca II features may be at least partially due to ejecta-CSM interaction (e.g., Mazzali et al. 2005; Tanaka et al. 2006). Therefore, if a link between these quantities was identified, it would provide evidence that blueshifted Na I D features are due to CSM also rather than contamination. We remind the reader that the two probes do explore different distances from the SN, with Ca II originating at significantly shorter distances than Na I D. However, when we examine the strength of the high-velocity Ca II components (parameterised through the Ca II  $R_{\text{HVF}}$  of Childress et al. 2013a) compared to the blueshifted Na I D<sub>2</sub> pEQW (15), we do not identify any clear trend between them. In particular, we also find that a number of SNe Ia with no Na I D absorption at all have very high Ca II  $R_{\text{HVF}}$  values, which is difficult to interpret in the context of a common CSM origin for both strong blueshifted Na I D features and strong high-velocity Ca II components, as with this interpretation of their origin a strong signature would be expected in both probes rather than singularly. We also find no correlation between the pEQW of the high-velocity Ca II features and the pEQW of the blue-shifted Na I D features.

Since we do not identify a link between the Na I D features and the strength of high-velocity Ca II features, this suggests that either one (or both) of these measurements are unrelated to CSM. Alternatively, these features may explore different regions of CSM, with Na I D absorption produced at much larger distances ( $10^{16} - 10^{17}$  cm) from the SN (e.g., Patat et al. 2007) than the CSM potentially probed through strong high-velocity Ca II absorption at  $< 10^{15}$  cm (Gerardy et al. 2004; Mulligan & Wheeler 2018). An alternative scenario that has been suggested for the high-velocity Ca II components is that they are due to a density or abundance enhancement in the SN ejecta (Branch et al. 2006; Blondin et al. 2012) and thus have no connection to the presence of CSM.

### 5.3 Can the excess of blueshifted Na I D be explained by CSM?

We have identified a clear excess of blueshifted over redshifted Na I D absorption features in both our new sample (33 per cent) and our full sample (24 per cent). Previous studies that have investigated these features have suggested that the most probable scenario to produce them is from CSM in the immediate vicinity of the SN (e.g., Sternberg et al. 2011; Maguire et al. 2012; Phillips et al. 2013). This conclusion was based on the original result of Patat et al. (2007), where time-varying Na I D features were observed in SN 2006X and were suggested to be due to changes in the ionisation field of the CSM caused by the SN radiation. This material was estimated to be located at a radius of  $\sim 10^{16}$  cm from the SN. Other SNe Ia were subsequently identified with these time-varying Na I D features and were also suggested to be due to CSM, most likely related to explosion scenarios involving non-degenerate companion stars (Simon et al. 2009; Blondin et al. 2009; Stritzinger et al. 2010; Sternberg et al. 2014). There are also models of double-degenerate systems that could eject material several thousand years prior to the explosion that interacts with the ISM, and also could potentially produce similar Na I D profiles (e.g., Raskin & Kasen

2013; Shen et al. 2013). However, it is likely that significant fine-tuning of double-degenerate models would be required to produce such material ejections in a large percentage of SNe Ia, as well as the host galaxy dependence of SNe Ia showing blueshifted Na I D absorption features towards late-time host galaxies being less easy to explain with this scenario. Double degenerate scenarios not having a strong preference for a particular stellar population compared to single degenerate models that require the younger stellar populations observed in late type galaxies.

In this study, we have investigated a number of SN Ia properties directly to see if the presence of blueshifted Na I D features are intrinsically linked to SNe Ia explosions. As discussed in Sections 5.1 and 5.2, there is a preference for the presence of Na I D in late-type host galaxies, which also results in a correlation with light-curve stretch, although the driving force behind these correlations is not well understood. We also observe the presence of the previously identified relation that SNe Ia with redder  $B-V$  colours at maximum have stronger Na I D features, though we observe this trend only in objects showing purely blueshifted absorption, with objects showing both blue and redshifted absorption found to have consistent  $B-V$  colours regardless of the strength of their blueshifted Na I D component. However, Phillips et al. (2013) showed that this is most likely driven by gas in the ISM and not due to CSM.

Related to the above, Phillips et al. (2013) investigated the connection between the Na I D column densities seen in SNe Ia and extinction measured from the SN colours, finding that those with stronger Na I D column densities, compared to the standard Milky Way-derived extinction relation, have preferentially blueshifted Na I D features and hence may have an origin in the CSM. However, there was not a clear correlation with some SNe Ia with identified time-varying Na I D not following the expected relation, suggesting that the situation is more complicated than previously thought and that strong blueshifted Na I D features may be produced in some way other than through CSM (under the assumption that time-varying Na I D are produced by CSM interaction).

The low  $R_V$  values seen in some SNe Ia have been attributed to multiple scatterings in CSM at typical radii ( $10^{16} - 10^{19}$  cm) (Wang 2005; Patat et al. 2006; Goobar 2008; Amanullah & Goobar 2011), while some more recent studies have investigated the presence of blueshifted Na I D features in the context of an origin in the ISM at  $10^{16} - 10^{20}$  cm (e.g. Bulla et al. 2018a,b).

These ISM-origin models are based on cloud-cloud collisions produced by SN radiation interacting with clouds in the ISM in the vicinity of the SN at  $\sim 10^{18}$  cm (Hoang et al. 2019). This mechanism would reduce the dust grain sizes (that would explain the lower  $R_V$ ) and could accelerate the clouds towards the observer (that would explain the preference for blueshifted Na I D features). This scenario, however, requires the IS cloud to be relatively close to the SN ( $\lesssim 1$  pc, see Figure 6 of Giang et al. 2020) in order to explain the low  $R_V$  values and blueshifted Na I D features observed already at early phases (pre-maximum). An acceleration of the blueshifted material with time would also be expected though has not been observed in SNe Ia, with blueshifted Na I D features having been observed to evolve in intensity but not in velocity. Newer models (Hoang 2021) suggest that interaction with SN radiation is not needed at all and these small dust grains could be produced by the ISM radiation alone before the SN explosion, which would resolve the timescale issue above. There are, however, some remaining issues with this model, including the lack of observations for similar polarisation laws in the Milky Way as observed for SNe Ia (Cikota et al. 2018) and a lack of quantitative estimates of the velocities expected for the gas (and not the dust grains) within the ISM that would give rise to the



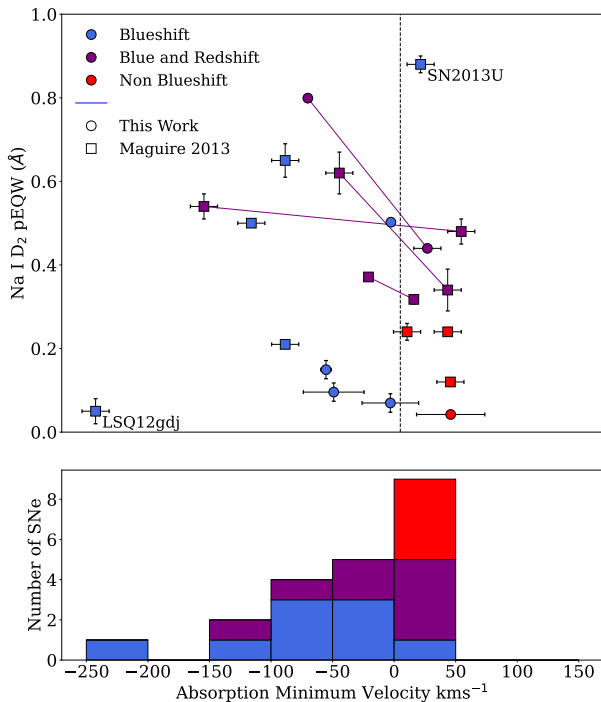


**Figure 16.** Top panel: Na I D pEQW absorption strength against the absorption minima velocity of the strongest component feature. In the case of ‘blue and redshifted’ objects, pEQW and the absorption minima velocities is measured in two regions ( $-200 - 0 \text{ km s}^{-1}$  and  $0 - 200 \text{ km s}^{-1}$ ) joined by connecting lines for the same object. SNe with other absorption classifications are measured across the full feature. Those objects showing no absorption features have been excluded. Objects originally presented in [Sternberg et al. \(2011\)](#) are not included due to differences in the velocity methodology. Bottom panel: The same data presented as a histogram to highlight the differences in distribution between Na I D absorption classification.

blueshifted Na I D features. These newer ISM only models also fail to explain why we see the clear excess in blueshifted over redshifted Na I D features that is once again seen to be statistically significant in both our new and full samples of now 47 SNe Ia with the requisite intermediate-resolution spectroscopy around maximum light.

Additionally, there appears to be tentative evidence of a possible distinction in the absorption minimum velocities of the Na I D features between the sub-classifications of absorption feature. With the minima of purely blueshifted absorption features, and the blueshifted components of those objects showing both blue and redshifted absorption, measured to be at higher relative velocities (Mean value:  $-51 \pm 62 \text{ km s}^{-1}$ ) compared to the absorption minima of redshifted absorption features as shown in Figure 16 (Mean value:  $22 \pm 12 \text{ km s}^{-1}$ ). The small number of objects makes drawing firm conclusions based on this difficult but could potentially be explained by a combination of a symmetric population around  $0 \text{ km s}^{-1}$  produced by distant ISM with an additional population at higher, bluer relative velocities produced by CSM or close-by ISM.

## 6 CONCLUSIONS

This work has explored a new sample of moderate-resolution spectra of 15 SNe Ia obtained near maximum light to investigate the potential link between the properties of narrow Na I D absorption features and high-velocity Ca II NIR triplet absorption features, with

the goal of constraining the progenitor scenarios of SNe Ia more firmly. Our main conclusions are:

- (i) we confirmed a %EB of 23 per cent blueshifted over redshifted Na I D features in a new sample of maximum-light SN Ia intermediate-resolution spectra, in agreement with previous studies,
- (ii) we found that this excess was even stronger (48 per cent) in a full sample of 47 SNe Ia (including literature objects) when only spiral/late-type host galaxies were considered,
- (iii) we did not identify a trend between the presence or strength of high-velocity Ca II features seen in the majority of SNe Ia around maximum light and the presence of narrow blueshifted Na I D features,
- (iv) we observed that the previous identified correlation that stronger blueshifted Na I D features are seen in SNe Ia displaying redder  $B-V$  colours at maximum light is present only for those objects displaying purely blueshifted absorption. No trend is observed for objects with blue and redshifted Na I D absorption,
- (v) we have identified a tentative relation that the velocity distribution of the narrow blueshifted Na I D features may extend to higher velocities than that of the non-blueshifted Na I D sample
- (vi) we found that SNe Ia in irregular galaxies do not show Na I D absorption at odds with their likely underlying stellar populations (although the sample size is very small)

The lack of a link between the properties of the narrow Na I D features and the high-velocity Ca II components around maximum light in SNe Ia suggests either that one or both of these probes is not due to CSM as has previously been suggested or the presence of CSM around Type Ia SNe cannot be linked across the range of distances explored by the two probes. However, the confirmation of a clear excess of blueshifted over redshifted Na I D absorption features in our new sample, and the full combined literature sample, cannot easily be explained through ISM interpretations of the Na I D feature that do not involve an impact of the SN progenitor system or ejecta on these features. Further theoretical modelling is required to provide new scenarios to explain these results, most likely either in the context of close-in ISM or CSM.

## ACKNOWLEDGEMENTS

PC and KM acknowledge support from the EU H2020 ERC grant no. 758638. MB acknowledges support from the Swedish Research Council (Reg. no. 2020-03330). L.G. acknowledges financial support from the Spanish Ministry of Science, Innovation and Universities (MICIU) under the 2019 Ramón y Cajal program RYC2019-027683 and from the Spanish MICIU project PID2020-115253GA-I00. SJS acknowledges funding from STFC Grants ST/P000312/1 and ST/N002520/1.

Based on data taken at the European Organization for Astronomical Research in the Southern Hemisphere, Chile, under program IDs: 098.D-0384(A) and 099.D-0641(A). This research has made use of the NASA/IPAC Extragalactic Database (NED) which is operated by the Jet Propulsion Laboratory, California Institute of Technology, under contract with the National Aeronautics and Space Administration.

This work has made use of data from the Asteroid Terrestrial-impact Last Alert System (ATLAS) project. ATLAS is primarily funded to search for near earth asteroids through NASA grants NN12AR55G, 80NSSC18K0284, and 80NSSC18K1575; byproducts of the NEO search include images and catalogs from the survey area. The ATLAS science products have been made possible through

the contributions of the University of Hawaii Institute for Astronomy, the Queen's University Belfast, the Space Telescope Science Institute, the South African Astronomical Observatory (SAAO), and the Millennium Institute of Astrophysics (MAS), Chile.

Funding for the Sloan Digital Sky Survey IV has been provided by the Alfred P. Sloan Foundation, the U.S. Department of Energy Office of Science, and the Participating Institutions. SDSS acknowledges support and resources from the Center for High-Performance Computing at the University of Utah. The SDSS web site is [www.sdss.org](http://www.sdss.org).

We thank the anonymous reviewer for their helpful comments and discussion.

## DATA AVAILABILITY

The data underlying this article will be shared on reasonable request to the corresponding author.

## REFERENCES

- Ahumada R., et al., 2020, *ApJS*, 249, 3
- Amanullah R., Goobar A., 2011, *ApJ*, 735, 20
- Amanullah R., et al., 2014, *ApJ*, 788, L21
- Astier P., et al., 2006, *A&A*, 447, 31
- Blanton M. R., et al., 2017, *AJ*, 154, 28
- Blondin S., Tonry J. L., 2007, in AIP Conference Proceedings. pp 312–321, [doi:10.1063/1.2774875](https://doi.org/10.1063/1.2774875)
- Blondin S., Prieto J. L., Patat F., Challis P., Hicken M., Kirshner R. P., Matheson T., Modjaz M., 2009, *ApJ*, 693, 207
- Blondin S., et al., 2012, *AJ*, 143, 126
- Blondin S., Prieto J. L., Patat F., Challis P., Hicken M., Kirshner R. P., Matheson T., Modjaz M., 2017, *ApJ*, 844, 88
- Branch D., et al., 2006, *PASP*, 118, 560
- Bulla M., Goobar A., Amanullah R., Feindt U., Ferretti R., 2018a, *MNRAS*, 473, 1918
- Bulla M., Goobar A., Dhawan S., 2018b, *MNRAS*, 479, 3663
- Burns C. R., et al., 2014, *ApJ*, 789
- Chambers K. C., et al., 2016, In Prep
- Childress M. J., Filippenko A. V., Ganeshalingam M., Schmidt B. P., 2013a, *MNRAS*, 437, 338
- Childress M. J., et al., 2013b, *ApJ*, 770
- Cikota A., et al., 2018, *A & A*, 615, A42
- Conley A., Carlberg R. G., Guy J., Howell D. A., Jha S., Riess A. G., Sullivan M., 2007, *ApJ*, 664, L13
- Conley A., et al., 2008, *ApJ*, 681, 482
- Doi M., et al., 2010, *AJ*, 139, 1628
- Ferretti R., Amanullah R., Bulla M., Goobar A., Johansson J., Lundqvist P., 2017, *ApJ*, 851, L43
- Fink M., Röpke F. K., Hillebrandt W., Seitenzahl I. R., Sim S. A., Kromer M., 2010, *A&A*, 514, 1
- Fitzpatrick E. L., 1999, *PASP*, 111, 63
- Foley R. J., et al., 2012, *ApJ*, 752, 101
- Förster F., González-Gaitán S., Anderson J., Marchi S., Gutiérrez C., Hamuy M., Pignata G., Cartier R., 2012, *ApJ Letters*, 754, 1
- Freudling W., Romaniello M., Bramich D. M., Ballester P., Forchi V., García-Dabó C. E., Moehler S., Neeser M. J., 2013, *A&A*, 559, A96
- Frohmaier C., et al., 2019, *MNRAS*, 486, 2308
- Fukugita M., Ichikawa T., Gunn J. E., Doi M., Shimasaku K., Schneider D. P., 1996, *AJ*, 111, 1748
- Galliano F., Galametz M., Jones A. P., 2018, *ARA&A*, 56, 673
- Gerardy C. L., et al., 2004, *ApJ*, 607, 391
- Giang N. C., Hoang T., Tram L. N., 2020, *ApJ*, 888, 93
- Goobar A., 2008, *ApJ*, 686, L103
- Grebel E. K., 2004, *Origin and Evolution of the Elements*, 4, 234
- Gunn J. E., et al., 1998, *AJ*, 116, 3040
- Gunn J. E., et al., 2006, *AJ*, 131, 2332
- Hachisu I., Kato M., Nomoto K., Umeda H., 1999a, *ApJ*, 519, 314
- Hachisu I., Kato M., Ichi Nomoto K., 1999b, *ApJ*, 522, 487
- Hamuy M., Phillips M. M., Maza J., Suntzeff N. B., Schommer R. A., Aviles R., 1995, *AJ*, 109, 1
- Hamuy M., Phillips M. M., Suntzeff N. B., Schommer R. A., Maza J., Aviles R., 1996, *AJ*, 112, 2391
- Hamuy M., Trager S. C., Pinto P. A., Phillips M. M., Schommer R. A., Ivanov V., Suntzeff N. B., 2000, *AJ*, 120, 1479
- Hatano K., Branch D., Fisher A., Baron E., Filippenko A. V., 1999, *ApJ*, 525, 881
- Hoang T., 2017, *ApJ*, 836, 13
- Hoang T., 2021, *ApJ*, 907, 37
- Hoang T., Tram L. N., Lee H., Ahn S.-h., 2019, *Nature Astronomy*, 3, 766
- Hosseinzadeh G., et al., 2017, *ApJ*, 845, L11
- Hunter D., 1997, *PASP*, 109, 937
- Hunter D. A., Elmegreen B. G., Martin E., 2006, *AJ*, 132, 801
- Jha S. W., Maguire K., Sullivan M., 2019, *Nature Astronomy*, 3, 706
- Kausch W., et al., 2015, *A&A*, 576, A78
- Lauberts A., Holmberg E., Schuster H.-E., West R., 1981, *A&AS*, 43, 307
- Li W., Chornock R., Leaman J., Filippenko A. V., Poznanski D., Wang X., Ganeshalingam M., Mannucci F., 2011, *MNRAS*, 412, 1473
- Livne E., Arnett D., 1995, *ApJ*, 452, 62
- Loveday J., 1996, *MNRAS*, 278, 1025
- Maguire K., et al., 2012, *MNRAS*, 426, 2359
- Maguire K., et al., 2013, *MNRAS*, 436, 222
- Maguire K., et al., 2014, *MNRAS*, 444, 3258
- Mandel K. S., Narayan G., Kirshner R. P., 2011, *ApJ*, 731
- Maoz D., Mannucci F., Nelemans G., 2014, *ARA&A*, 52, 107
- Mazzali P. A., et al., 2005, *ApJ*, 623, L37
- Mazzei P., Marino A., Rampazzo R., Plana H., Rosado M., Arias L., 2018, *A&A*, 610, A8
- Modigliani A., et al., 2010, in *Observatory Operations: Strategies, Processes, and Systems III*. SPIE, pp 773728–773728, [doi:10.1117/12.857211](https://doi.org/10.1117/12.857211)
- Mörtzell E., 2013, *A&A*, 550, A80
- Mulligan B. W., Wheeler J. C., 2018, *MNRAS*, 476, 1299
- Nataf D. M., et al., 2013, *ApJ*, 769, 88
- Pakmor R., Kromer M., Röpke F. K., Sim S. A., Rüter A. J., Hillebrandt W., 2010, *Nature*, 463, 61
- Pan Y. C., et al., 2014, *MNRAS*, 438, 1391
- Patat F., Benetti S., Cappellaro E., Turatto M., 2006, *MNRAS*, 369, 1949
- Patat F., et al., 2007, *Science*, 317, 924
- Patat F., et al., 2015, *A&A*, 577, 1
- Phillips M. M., et al., 2013, *ApJ*, 779
- Quimby R., Hoflich P., Kannappan S. J., Rykoff E., Rujopakarn W., Akerlof C. W., Gerardy C. L., Wheeler J. C., 2006, *ApJ*, 636, 400
- Raskin C., Kasen D., 2013, *ApJ*, 772, 1
- Riess A. G., et al., 1999, *AJ*, 117, 707
- Rigault M., et al., 2018, *A&A*
- Sand D., Valenti S., Tartaglia L., Yang S., Wyatt S., 2018, in *American Astronomical Society Meeting Abstracts #231*. pp 245.11–245.11
- Schlafly E. F., Finkbeiner D. P., 2011, *ApJ*, 737
- Schwarz G., 1978, *The Annals of Statistics*, 6, 1403
- Scolnic D. M., et al., 2018, *ApJ*, 859, 101
- Shappee B., et al., 2014, in *American Astronomical Society Meeting Abstracts #223*. pp 236.03–236.03
- Shen K. J., Bildsten L., 2009, *ApJ*, 699, 1365
- Shen K. J., Guillochon J., Foley R. J., 2013, *ApJ Letters*, 770, 1
- Shingles L., et al., 2021, *Transient Name Server AstroNote*, 7
- Simon J. D., et al., 2009, *ApJ*, 702, 1157
- Smette A., et al., 2015, *A&A*, 576, A77
- Smith K. W., et al., 2020, *PASP*, 132, 85002
- Sternberg A., et al., 2011, *Science*, 333, 856
- Sternberg A., et al., 2014, *MNRAS*, 443, 1849
- Stritzinger M., et al., 2010, *AJ*, 140, 2036
- Sullivan M., et al., 2010, *MNRAS*, 406, 782
- Taam R. E., 1980, *ApJ*, 242, 749

- Tanaka M., Mazzali P. A., Maeda K., Nomoto K., 2006, *ApJ*, 645, 470  
Tanaka M., et al., 2008, *ApJ*, 677, 448  
Taylor E. N., et al., 2011, *MNRAS*, 418, 1587  
Tonry J. L., et al., 2018, *PASP*, 130, 64505  
Vernet J., et al., 2011, *A&A*, 536, A105  
Wang L., 2005, *ApJ*, 635, L33  
Wang X., et al., 2009, *ApJ*, 699, L139  
Whelan J., Iben Jr. I., Iben Jr. I., 1973, *ApJ*, 186, 1007  
Zelaya P., et al., 2017, *ApJ*, 836, 88  
de Vaucouleurs G., de Vaucouleurs A., Corwin H. G., Buta R. J., Paturel G., Fouqué P., 1991, *Third Reference Catalogue of Bright Galaxies*. Springer New York, New York, NY, doi:10.1007/978-1-4757-4360-9

**APPENDIX A: LITERATURE OBJECTS: BROAD FEATURE FITTING RESULTS**

For objects identified as not displaying a high velocity feature in their spectrum the ‘Fitting Notes’ column of the following tables details the first criterion each spectrum failed to meet. These criteria are described in more detail in Section 3.3.2 but are outlined here for clarity:

- (i) The fitting of a high velocity feature must be successful in at least 10% of iterations.
- (ii) The inclusion of a high velocity feature must be strongly favoured by the BIC indicated by a  $\Delta\text{BIC}$  value  $>10$ .

This paper has been typeset from a  $\text{\TeX}/\text{\LaTeX}$  file prepared by the author.

**Table A1.** Summarised fitting results for the  $\text{Si II } 6355 \text{ \AA}$  feature for the objects first described in Maguire et al. (2013). Means have been weighted using the relevant fitting uncertainties with the uncertainties of these means obtained as the standard deviation of the results. A positive value of  $\Delta\text{BIC}$  indicates a preference for the inclusion of a high velocity feature based on statistical considerations alone.

No High Velocity component									
SN	Photospheric Component			High Velocity Component			$\bar{\chi}^2$	$\Delta\text{BIC}$	Fitting Notes
	Min V ( $\text{km s}^{-1}$ )	FWHM ( $\text{km s}^{-1}$ )	pEQW ( $\text{\AA}$ )	Min V ( $\text{km s}^{-1}$ )	FWHM ( $\text{km s}^{-1}$ )	pEQW ( $\text{\AA}$ )			
LSQ12fxd	$-11150 \pm 50$	$6830 \pm 100$	$74.7 \pm 1$	-	-	-	$0.251 \pm 0.017$	*	(1), (i)
PTF12iiq	$-18980 \pm 220$	$10640 \pm 880$	$58.4 \pm 5.7$	-	-	-	$2.973 \pm 0.626$	$-10 \pm 140$	(1), (ii)
SN 2012hd	$-10070 \pm 180$	$7510 \pm 180$	$31.0 \pm 0.0$	-	-	-	$0.119 \pm 0.001$	$90 \pm 30$	(1), (i)
SN 2013U	$-9980 \pm 50$	$7910 \pm 70$	$56.3 \pm 0.5$	-	-	-	$0.527 \pm 0.005$	$-40 \pm 40$	(ii)
SN 2013aj	$-11060 \pm 50$	$7750 \pm 50$	$118.1 \pm 0.1$	-	-	-	$0.113 \pm 0.005$	*	(i)
Mean	$-11250 \pm 3400$	$7650 \pm 1310$	$55.6 \pm 28.8$	-	-	-	$0.192 \pm 1.098$	$0 \pm 40$	
With High Velocity component									
SN	Photospheric Component			High Velocity Component			$\bar{\chi}^2$	$\Delta\text{BIC}$	Fitting Notes
	Min V ( $\text{km s}^{-1}$ )	FWHM ( $\text{km s}^{-1}$ )	pEQW ( $\text{\AA}$ )	Min V ( $\text{km s}^{-1}$ )	FWHM ( $\text{km s}^{-1}$ )	pEQW ( $\text{\AA}$ )			
LSQ12dbr	$-11120 \pm 400$	$6140 \pm 150$	$64.9 \pm 8.5$	$-13320 \pm 140$	$3020 \pm 480$	$10.5 \pm 8.5$	$0.130 \pm 0.019$	$290 \pm 70$	
LSQ12fuk	$-9690 \pm 50$	$6180 \pm 60$	$83.3 \pm 0.1$	$-12610 \pm 50$	$3070 \pm 70$	$8.6 \pm 0.1$	$0.074 \pm 0.001$	$260 \pm 50$	
LSQ12gdj	$-10910 \pm 280$	$5420 \pm 250$	$10.3 \pm 0.8$	$-12590 \pm 210$	$2340 \pm 390$	$1.2 \pm 0.8$	$0.006 \pm 0.001$	$60 \pm 20$	(1)
LSQ12hzj	$-8230 \pm 380$	$6890 \pm 160$	$51.7 \pm 5.4$	$-10440 \pm 110$	$4320 \pm 360$	$25.1 \pm 5.4$	$0.145 \pm 0.012$	$340 \pm 50$	
PTF12jgb	$-8950 \pm 400$	$5410 \pm 370$	$43.4 \pm 8.2$	$-11900 \pm 200$	$4120 \pm 490$	$23.2 \pm 8.2$	$0.037 \pm 0.002$	$230 \pm 80$	(1)
SN 2012cg	$-9710 \pm 120$	$6710 \pm 70$	$50.9 \pm 3.1$	$-11650 \pm 120$	$4660 \pm 220$	$24.2 \pm 3.1$	$0.041 \pm 0.001$	$410 \pm 50$	
SN 2012fw	$-10280 \pm 430$	$6030 \pm 300$	$11.1 \pm 1.9$	$-12160 \pm 360$	$3510 \pm 700$	$2.6 \pm 1.9$	$0.015 \pm 0.001$	$50 \pm 20$	(1)
SN 2012hr	$-12470 \pm 90$	$8390 \pm 100$	$74.1 \pm 0.6$	$-16350 \pm 200$	$3270 \pm 370$	$5.7 \pm 0.6$	$0.114 \pm 0.025$	$260 \pm 40$	(1)
SN 2012ht	$-9940 \pm 60$	$6660 \pm 70$	$76.8 \pm 1.3$	$-13310 \pm 50$	$4890 \pm 80$	$33.8 \pm 1.3$	$0.045 \pm 0.002$	$600 \pm 50$	
SN 2013aa	$-9750 \pm 360$	$5650 \pm 250$	$77.4 \pm 10.5$	$-12220 \pm 190$	$2780 \pm 640$	$16.2 \pm 10.5$	$0.106 \pm 0.014$	$480 \pm 100$	
Mean	$-10250 \pm 1120$	$6570 \pm 840$	$69 \pm 25.1$	$-12650 \pm 1460$	$3810 \pm 810$	$9.7 \pm 10.5$	$0.034 \pm 0.047$	$220 \pm 160$	

\* No  $\Delta\text{BIC}$  is available for these objects as all fitting iterations when including a high velocity feature were considered to be unsuccessful

(1) Values measured from a lower resolution, non X-shooter spectrum

Roman numerals denote the first fitting criterion failed by each object not identified as displaying a high velocity feature, as described in Section 3.3.2

**Table A2.** Summarised fitting results for the Ca II NIR triplet feature for the objects first described in Maguire et al. (2013). Means have been weighted using the relevant fitting uncertainties with the uncertainties of these means obtained as the standard deviation of the results. A positive value of  $\Delta\text{BIC}$  indicates a preference for the inclusion of a high velocity feature based on statistical considerations alone.

No High Velocity component									
SN	Photospheric Component			High Velocity Component			$\bar{\chi}^2$	$\Delta\text{BIC}$	Fitting Notes
	Min V (km s <sup>-1</sup> )	FWHM (km s <sup>-1</sup> )	pEQW (Å)	Min V (km s <sup>-1</sup> )	FWHM (km s <sup>-1</sup> )	pEQW (Å)			
LSQ12gdj	-11000 ± 130	3180 ± 140	6.0 ± 0.1	-	-	-	0.245 ± 0.001	40 ± 20	(1), (i)
PTF12iic	-32170 ± 120	32160 ± 310	220.5 ± 1.1	-	-	-	24.642 ± 0.486	*	(1), (i)
SN 2013U	-14440 ± 50	16200 ± 60	48.4 ± 0.4	-	-	-	1.768 ± 0.003	*	(i)
Mean	-18070 ± 9270	14610 ± 11850	23.0 ± 92.7	-	-	-	0.729 ± 11.159	-	
With High Velocity component									
SN	Photospheric Component			High Velocity Component			$\bar{\chi}^2$	$\Delta\text{BIC}$	Fitting Notes
	Min V (km s <sup>-1</sup> )	FWHM (km s <sup>-1</sup> )	pEQW (Å)	Min V (km s <sup>-1</sup> )	FWHM (km s <sup>-1</sup> )	pEQW (Å)			
LSQ12dbr	-11040 ± 110	4430 ± 40	55.3 ± 0.3	-18680 ± 40	4780 ± 60	32.6 ± 0.3	1.009 ± 0.007	500 ± 60	
LSQ12fuk	-9500 ± 40	5300 ± 40	104.6 ± 0.1	-16840 ± 40	4680 ± 40	55.3 ± 0.1	0.636 ± 0.001	1090 ± 60	
LSQ12fxd	-10800 ± 140	2810 ± 140	9.3 ± 0.2	-21340 ± 130	5670 ± 140	23.2 ± 0.1	0.375 ± 0.009	270 ± 20	(1)
LSQ12hzj	-8390 ± 300	4500 ± 40	46.1 ± 0.2	-18710 ± 40	6040 ± 50	29.5 ± 0.2	1.354 ± 0.003	480 ± 50	
PTF12jgb	-9430 ± 170	5280 ± 160	67.2 ± 9.6	-18510 ± 750	5580 ± 1630	56.8 ± 9.8	0.516 ± 0.245	1060 ± 170	(1)
SN 2012cg	-9980 ± 40	4440 ± 40	51.1 ± 0.1	-19510 ± 100	5550 ± 40	52.5 ± 0.1	0.558 ± 0.002	1000 ± 60	
SN 2012fw	-9390 ± 190	4610 ± 190	13.5 ± 0.1	-18480 ± 210	5590 ± 190	11.2 ± 0.1	0.406 ± 0.012	100 ± 20	(1)
SN 2012hd	-9730 ± 140	7390 ± 140	47.0 ± 0.1	-17490 ± 170	5920 ± 140	31.6 ± 0.1	0.365 ± 0.005	240 ± 30	(1)
SN 2012hr	-12400 ± 80	8890 ± 140	107.2 ± 1.6	-20250 ± 120	6540 ± 100	68.7 ± 1.3	1.071 ± 0.026	260 ± 50	(1)
SN 2012ht	-10860 ± 40	7490 ± 40	145.6 ± 0.7	-17400 ± 10	6960 ± 60	67.5 ± 0.7	0.629 ± 0.005	390 ± 70	
SN 2013aa	-9880 ± 30	5700 ± 30	119.7 ± 0.1	-15840 ± 100	4840 ± 40	42.9 ± 0.1	1.132 ± 0.002	340 ± 60	
SN 2013aj	-9810 ± 40	6440 ± 40	100.1 ± 0.2	-17110 ± 40	9240 ± 40	102 ± 0.2	1.288 ± 0.004	570 ± 100	
Mean	-10180 ± 990	5600 ± 1610	52.7 ± 41.0	-17810 ± 1470	6020 ± 1190	36.3 ± 23.7	0.813 ± 0.352	380 ± 320	

\* No  $\Delta\text{BIC}$  is available as all fitting iterations when including a high velocity feature were considered to be unsuccessful

\*\* Residual pattern indicative of the presence of an additional feature

(1) Values measured from a lower resolution, non X-shooter spectrum

Roman numerals denote the first fitting criterion failed by each object not identified as displaying a high velocity feature, as described in Section 3.3.2

**Table A3.** Summarised fitting results for the Si II 6355 Å feature for the objects first described in Sternberg et al. (2011). Means have been weighted using the relevant fitting uncertainties with the uncertainties of these means obtained as the standard deviation of the results. A positive value of  $\Delta\text{BIC}$  indicates a preference for the inclusion of a high velocity feature based on statistical considerations alone.

No High Velocity component									
SN	Photospheric Component			High Velocity Component			$\bar{\chi}^2$	$\Delta\text{BIC}$	Fitting Notes
	Min V (km s <sup>-1</sup> )	FWHM (km s <sup>-1</sup> )	pEQW (Å)	Min V (km s <sup>-1</sup> )	FWHM (km s <sup>-1</sup> )	pEQW (Å)			
SN 2006cm	-11350 ± 90	4850 ± 170	24.9 ± 0.8	-	-	-	0.325 ± 0.012	*	(1), (i)
SN 2008hv	-11080 ± 100	7450 ± 100	48.8 ± 0.3	-	-	-	0.037 ± 0.002	90 ± 20	(1), (i)
SN 2008ia	-11270 ± 100	7140 ± 120	53.7 ± 0.6	-	-	-	0.080 ± 0.005	-60 ± 40	(1), (ii)
SN 2009ig	-13700 ± 210	6540 ± 210	18.2 ± 0.0	-	-	-	0.050 ± 0.001	*	(1), (i)
Mean	-11560 ± 1070	6680 ± 1000	22.8 ± 15.1	-	-	-	0.061 ± 0.117	-10 ± 50	
With High Velocity component									
SN	Photospheric Component			High Velocity Component			$\bar{\chi}^2$	$\Delta\text{BIC}$	Fitting Notes
	Min V (km s <sup>-1</sup> )	FWHM (km s <sup>-1</sup> )	pEQW (Å)	Min V (km s <sup>-1</sup> )	FWHM (km s <sup>-1</sup> )	pEQW (Å)			
SN 2006X	-15710 ± 410	8420 ± 430	134.4 ± 13.9	-20430 ± 290	4830 ± 540	36.2 ± 13.9	0.148 ± 0.085	1000 ± 170	
SN 2007on	-9930 ± 140	6950 ± 150	27.3 ± 0.1	-13430 ± 140	4580 ± 140	11.8 ± 0.1	0.036 ± 0.001	250 ± 20	(1)
SN 2008fp	-10740 ± 150	6420 ± 150	21.8 ± 0.3	-12410 ± 180	3460 ± 380	2.7 ± 0.3	0.023 ± 0.003	90 ± 20	(1)
Mean	-11130 ± 2550	6940 ± 850	26.2 ± 51.9	-14590 ± 3570	4360 ± 600	9.1 ± 14.2	0.033 ± 0.056	220 ± 400	

\* No  $\Delta\text{BIC}$  is available as all fitting iterations when including a high velocity feature were considered to be unsuccessful

(1) Values measured from a lower resolution, non X-shooter spectrum

Roman numerals denote the first fitting criterion failed by each object not identified as displaying a high velocity feature, as described in Section 3.3.2



**Table A4.** Summarised fitting results for the Ca II NIR triplet feature for the objects first described in [Sternberg et al. \(2011\)](#). Means have been weighted using the relevant fitting uncertainties with the uncertainties of these means obtained as the standard deviation of the results. A positive value of  $\Delta\text{BIC}$  indicates a preference for the inclusion of a high velocity feature based on statistical considerations alone.

No High Velocity component									
SN	Photospheric Component			High Velocity Component			$\chi^2$	$\Delta\text{BIC}$	Fitting Notes
	Min V (km s <sup>-1</sup> )	FWHM (km s <sup>-1</sup> )	pEQW (Å)	Min V (km s <sup>-1</sup> )	FWHM (km s <sup>-1</sup> )	pEQW (Å)			
SN 2006cm	-11790 ± 70	7660 ± 70	61.1 ± 0.1	-	-	-	1.534 ± 0.007	*	(1), (i)
Mean	-	-	-	-	-	-	-	-	-
With High Velocity component									
SN	Photospheric Component			High Velocity Component			$\chi^2$	$\Delta\text{BIC}$	Fitting Notes
	Min V (km s <sup>-1</sup> )	FWHM (km s <sup>-1</sup> )	pEQW (Å)	Min V (km s <sup>-1</sup> )	FWHM (km s <sup>-1</sup> )	pEQW (Å)			
SN 2006X	-13330 ± 40	6490 ± 50	128.1 ± 0.9	-20030 ± 40	6440 ± 60	177.5 ± 1.3	0.753 ± 0.027	1030 ± 60	
SN 2007on	-8640 ± 160	6680 ± 150	24.6 ± 2.1	-14220 ± 200	9360 ± 200	51.4 ± 2.1	0.143 ± 0.003	120 ± 30	(1)
SN 2008fp	-10510 ± 110	5320 ± 110	20.6 ± 0	-17860 ± 150	4660 ± 110	7.9 ± 0.0	0.111 ± 0.004	210 ± 20	(1)
SN 2008hv	-9850 ± 70	5850 ± 70	34.1 ± 0.1	-19140 ± 70	7050 ± 90	20.0 ± 0.1	0.241 ± 0.002	480 ± 30	(1)
SN 2008ia	-9970 ± 70	5760 ± 70	48.1 ± 0.1	-17720 ± 120	6090 ± 70	21.9 ± 0.1	0.855 ± 0.003	200 ± 30	(1)
SN 2009ig	-13500 ± 160	6060 ± 160	21.5 ± 0	-21650 ± 160	4890 ± 160	4.5 ± 0.0	0.045 ± 0.001	240 ± 10	(1)
Mean	-11330 ± 1820	6040 ± 450	28 ± 37.9	-19070 ± 2310	6290 ± 1560	11.5 ± 60.2	0.233 ± 0.322	290 ± 310	

\* No  $\Delta\text{BIC}$  is available as all fitting iterations when including a high velocity feature were considered to be unsuccessful

\*\* Residual pattern indicative of the presence of an additional feature

(1) Values measured from a lower resolution, X-shooter spectrum

Roman numerals denote the first fitting criterion failed by each object not identified as displaying a high velocity feature, as described in Section 3.3.2